RESEARCH ARTICLE

Trace elements of pyrite and S, H, O isotopes from the Laowan gold deposit in Tongbai, Henan Province, China: implications for ore genesis

Yuehua ZHAO[1], Shouyu CHEN (✉)[1,2], Jianli CHEN[3], Shuaiji WU[1]

1 Faculty of Earth Resources, China University of Geosciences, Wuhan 430074, China
2 State Key Laboratory of Geological Processes and Mineral Resources, China University of Geosciences, Wuhan 430074, China
3 No. 1 Geological Exploration Institute, Henan Bureau of Geo-exploration and Mineral Development, Zhengzhou 450001, China

Abstract The Laowan deposit is a large gold deposit in the Qinling-Dabie orogenic belt where pyrite is the main Au-bearing mineral phase. We present results from the occurrences of gold, trace elements and sulfur isotopes of pyrite, and hydrogen and oxygen isotopes of quartz and calcite to elucidate the sources of ore-forming fluid; the genesis of pyrite and the ore-forming process.

From field observations, five generations of pyrite are identified; one formed in a metamorphic-diagenetic epoch (PyI), and the others during four mineralization stages: 1) the coarse-grained pyrite-quartz stage (PyII), 2) the quartz and medium- to fine-grained pyrite stage (PyIII), 3) the polymetallic sulfide stage (PyIV), and 4) the carbonate-quartz stage (PyV). Gold mainly occurs in PyIII and PyIV. We find that Au, Ag, Pb, and Cu are incorporated into pyrite as micro-/nano-inclusions and that Co, Ni, As, and Se enter the pyrite lattice via isomorphous replacement.

The Co/Ni values and Se concentrations indicate that PyI formed from metamorphic hydrothermal fluids and that pyrites (PyII, PyIII, and PyIV) from the ore-forming stages typically reflect a hydrothermal genesis involving magmatic fluid.

The $\delta^{34}S$ values of PyI (1.45 ‰–2.09 ‰) are similar to that of plagioclase amphibole schist, indicating that S was primarily derived from wall rock, while those of PyII, PyIII, and PyIV (3.10 ‰–5.55 ‰) suggest that S was derived from the Guishanyan Formation and the Laowan granite. The four mineralization stages show a systematic decrease in δD (from −77.1 ‰ to −82.8 ‰, −84.7 ‰, and −102.7 ‰), while the $\delta^{18}O_{H_2O}$ values showed a gradual decrease from 5.7 to 2.7 ‰, 1.0 ‰, and −1.3 ‰.

These data show that the ore-forming fluid was similar to a mixture of magmatic and meteoric waters. Thus, we conclude that the Laowan gold deposit is related to magmatic-hydrothermal fluid.

1 Introduction

The Laowan metallogenic belt is located in the eastern segment of the E-W-trending Qinling-Dabie orogenic belt, located between the North China Craton and the Yangtze Craton (Fig. 1(a)). The Laowan metallogenic belt is a narrow strip nearly 20 km long from north to south and 1.5 to 2.5 km wide (Fig. 1(b)). The Laowan gold deposit, a typical large ore deposit in this belt, is composed of the Laowan and Shangshanghe ore blocks (Gao, 1989; Ma, 2007; Chen et al., 2009). New exploration data indicate that the control depths of the ore bodies increased from −350 m to −1150 m and that the quantity of Au reserves reach more than 100 t at Au grades of 3.75–6.77 g/t (Zhou, 2016).

Numerous studies have investigated the Laowan gold deposit since its discovery, with most focusing on the relationship between the Laowan granite and its mineralization, sources of ore-forming material, and genetic type (Zhao, 1990; Shao, 1995; Xie et al., 2000, 2001, 2003, and 2005; Pan and Yue, 2002; Fang and Hou, 2004; He and Wang, 2005; Wang and Xu, 2005; Li, 2007; Zhang et al., 2008b; Yang et al., 2014a and 2014b; Kou et al., 2016; Kou, 2016). Despite a number of previous studies, the genesis of this deposit remains controversial. The main dispute is whether gold metallogenesis had a close genetic relationship with Yanshanian magmatism (Pan, 1999;
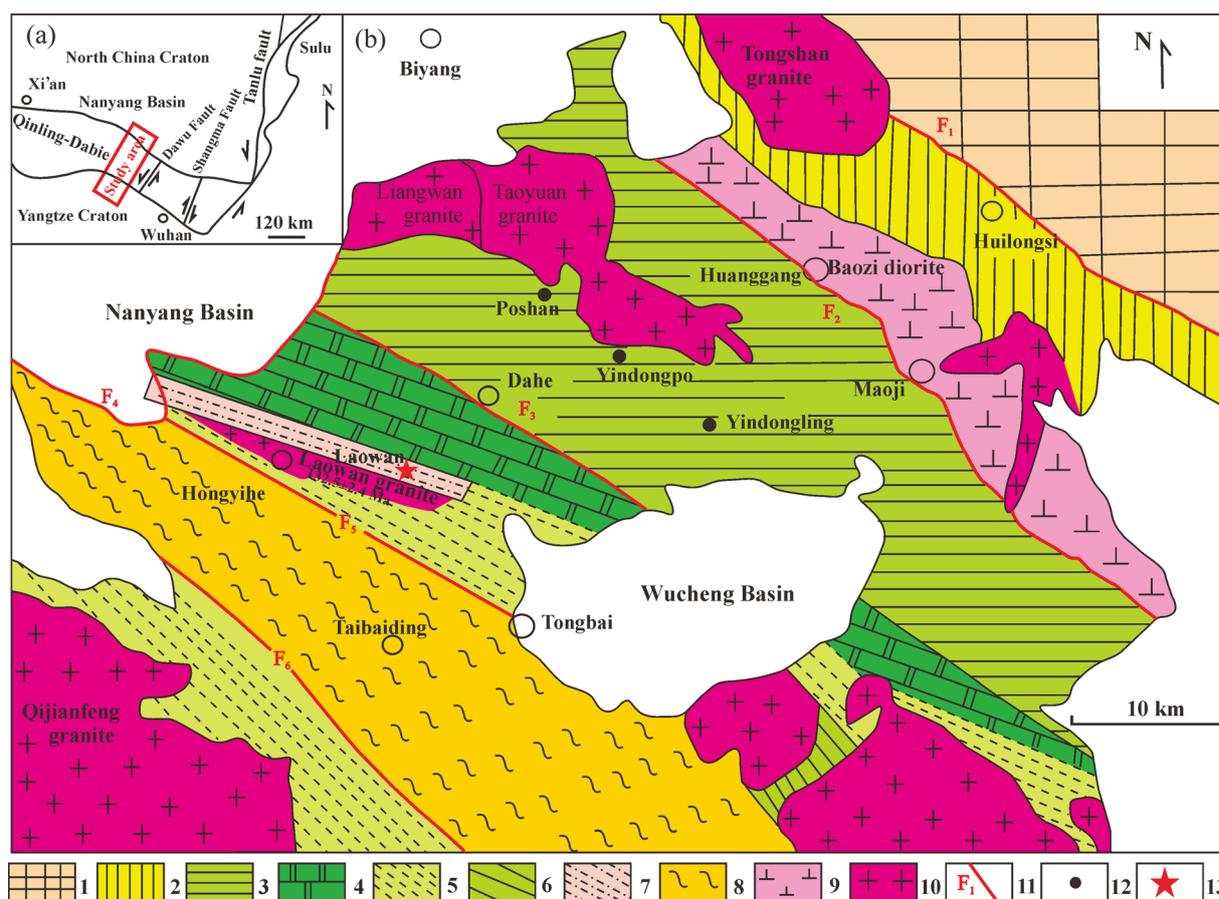
Fig. 1 Regional geological map of the Laowan gold belt (modified from Liu et al., 2011; Yang et al., 2014b). 1—Nanwan Formation; 2—Guishanyan Formation; 3—Kuanping Group; 4—Erlangping Group; 5—Qinling Group; 6—Xionger Group; 7—Tongbai metamorphic gneissic complex; 8—High pressure rock pile; 9—Diorite; 10—Granite; 11—Fault; 12—Gold-silver deposit; 13—Study area F₁—Youfangzhuang fault; F₂—Waxuezi fault; F₃—Zhuxia fault; F₄—Laowan-Songpa fault (Gui-Mei fault); F₅—Tongbai-Shangcheng fault; F₆—Xincheng-Huangpi fault

Yang et al., 2014b; Vikent'ev et al., 2015; Yang et al., 2015) or with tectonic activity in collisional orogenic belts through geological time (Zhang et al., 2002; Liu et al., 2003; Lin et al., 2010).

Even though past research on the Laowan gold deposit has resulted in the accumulation of abundant data on the geochemistry, sources of the ore-forming fluid, and isotopic compositions of the deposit, no research has been conducted on the trace element compositions of the sulfides and the occurrence of Au in the deposit. Pyrite is the main metal sulfide in the Laowan gold deposit, and it exhibits a close genetic relationship with Au enrichment and mineralization. Moreover, as the main Au-bearing mineral, studying the concentrations and associations of trace elements in hydrothermal pyrite can provide for a better understanding of the ore-forming processes and their physicochemical conditions (Li et al., 2004; Zheng et al., 2013). Additionally, many studies have shown that the typomorphic characteristics and compositions of pyrite can provide significant information about enrichment in Au (Cook et al., 2009; Large et al., 2009; Sung et al., 2009; Zhao et al., 2011; Zheng et al., 2013; Zhang et al., 2014;

Mills et al., 2015). Therefore, increased knowledge of the genesis and trace element composition of pyrite may provide useful information on the ore-forming fluid and the ore-forming process.

In this contribution, we report the results of trace element and S isotope analyses of pyrite obtained via laser ablation inductively coupled plasma mass spectrometry (LA-ICP-MS) and scanning electron microscopy (SEM). We also discuss the occurrence and concentrations of trace elements in pyrite and the associations of elements closely related to Au. Combing these data with hydrogen and oxygen isotopes, we present a new understanding of the ore-forming process and ore genesis.

2 Geological setting

2.1 Regional geological setting

The 1000-km-long Qinling-Dabie orogenic belt is located within a fold belt positioned along the southern margin of the North China Craton, and bounded by the Chenghui

basin to the west and the Tanlu fault to the east (Fig. 1(a)). This orogenic belt was caused by the collision between the southern active continental margin of the North China Craton and the northern passive continental margin of the Yangtze Craton. This region features a complex tectonic history (Dong et al., 2008) and abundant mineral resources. The Tongbai orogenic belt is located in the central-eastern part of the Qinling-Dabie orogenic belt (Zhao, 2007; Yuan and Li, 2008). The Laowan metallogenic belt, located in the central part of the Tongbai orogenic belt, is north of Tongbai Mountain (Fang and Hou, 2004) and adjacent to the Nanyang Basin to the west and the Wucheng Basin to the east (Fig. 1(b)) (Suo et al., 2002). It is 20 km long and 1.5–2.5 km wide (Yang et al., 2015) and bounded by the Songpa fault to the north and the Laowan fault to the south (Fig. 1). Due to the unique geological background, complex structure, and superior metallogenic conditions of the Laowan metallogenic belt, many ore deposits have been formed (Zhong et al., 2001). The study area of the "Laowan gold deposit" represents an important large Au deposit in this metallogenic belt.

Due to the superimposed deformation caused by multiple tectonic and metamorphic episodes, the regional strata primarily consist of a set of strongly deformed medium- to high-grade metamorphic and disordered rock series that were zonally distributed and formed during the Paleoproterozoic to the Cenozoic (Henan Geology and Mineral Bureau, 1989; Wang et al., 2009). The exposed strata mainly comprise the Kuanping Group, Erlangping Group, Qinling Group, Guishanyan Formation, and Nanwan Formation (Zhang et al., 2001) (Fig. 1(b)). The Kuanping Group comprises mica schists, quartzites, marbles, and amphibolites. Based on its preliminary isotopic ages, the Kuanping Group has been interpreted to have been metamorphosed during the late Proterozoic or Paleozoic (Zhang et al., 1991; Zhang et al., 1994). The Erlangping Group, which contains Paleozoic fossils (Niu et al., 1993), is a metavolcanic complex consisting of abundant upper greenschist-facies to amphibolite-facies rocks, whose protoliths may have been mafic to intermediate volcanic rocks and hypabyssal dikes (Zhang et al., 1989). The Qinling Group includes felsic and mafic granulites, amphibolites, granitoid gneisses, marbles, and subordinate metapelites. Its $^{207}Pb/^{206}Pb$ zircon ages range from 434 to 475 Ma (Kröner et al., 1993). The Guishanyan Formation is composed of plagioclase amphibole schist, biotite quartz schist, metamorphic quartzite, mylonites, and gneisses. Its age of metamorphism has been determined to be 470 Ma (Liu et al., 2010). The Nanwan Formation consists of sericite schist, amphibolite and muscovite schist, which are distributed on the south side of the Laowan granite.

The fault structures are relatively well-developed in this area, and the observed tectonic framework shows a NW-trending distribution. The faults closely related to the mineralization include the Tong-Shang, Gui-Mei (Songpa), Laowan and Dahe faults. The Tong-Shang fault is part of the strongly deformed Triassic plate suture zone (Suo and Zhang, 1993). The fracture is inclined to the south or to the north, with its inclination ranging from 70°–80°. This fault is characterized by a mylonite belt that is hundreds of meters to several kilometers wide (Chou et al., 1983). The Gui-Mei fault is an important rock- and ore-controlling structure in the Tongbai-Dabie orogenic belt, which is referred to as the Songpa fault in the study area (Suo et al., 2001). The Songpa fault is one of the most important faults in the Laowan gold deposit; it is located in the northern part of the area and is approximately 20 km long. This fault has had a long period of activity, with frequent tectonic movements (Shao, 1995). The Laowan fault, located in the southern part of the Laowan gold deposit, is also one of the most important faults. The fault structure is complex and exhibits multiple stages, with strikes ranging from 260°–280°; it is nearly 20 km long and also controlled the intrusion of the Laowan granite. In terms of the Dahe fault, the part of the fault located in the western region of the Nanyang Basin, is called the Zhuxia fault. The Erlangping Group is located on the north-eastern side of the fault, and the Qinling Group is located on its south-western side. A several hundred meters-long tectonic melange zone extends along the fault (Zhang et al., 2012).

The widespread igneous rocks in this area range from Archean volcanic rocks to Cenozoic granites. Based on previous studies, Mesozoic calc-alkaline granitoids and volcanic-intrusive potassic basaltic rocks may be closely associated with the mineralization. The magmatic rocks in this region mainly consist of Taoyuan medium-grained biotite granite, Liangwan biotite granite, Laofenpa granite stock, and Laowan biotite granite, as well as minor granitic porphyry, porphyry dikes, and lamprophyres.

2.2   Deposit geology

The Laowan gold deposit, one of the important deposits in the Laowan metallogenic belt, contains Au reserves reaching the scale of a large Au deposit (a defined reserve of approximately > 100 t Au at 3.75–6.77 g/t). The exposed strata in the Laowan gold deposit primarily comprise the Paleoproterozoic Qinling Group and Yanlinggou Formation, the Mesoproterozoic Guishanyan Formation, and the Cenozoic Quaternary (Fig. 2). The Guishanyan Formation is the principal ore-hosting stratum and is composed of plagioclase amphibole schist with some metamorphic gabbro dikes, two-mica quartz schist, leptynite, and plagiogneiss. It strikes NW with a dip angle of 48°–82°. The protolith of this unit was a set of intermediate to basic volcanic rocks and clastic rocks, both of which experienced regional greenschist-facies to lower amphibolite-facies metamorphism (Liu et al., 2010; Yang et al., 2015).

The Laowan and Songpa faults are boundary faults of the ore-controlling fault system in the Laowan gold
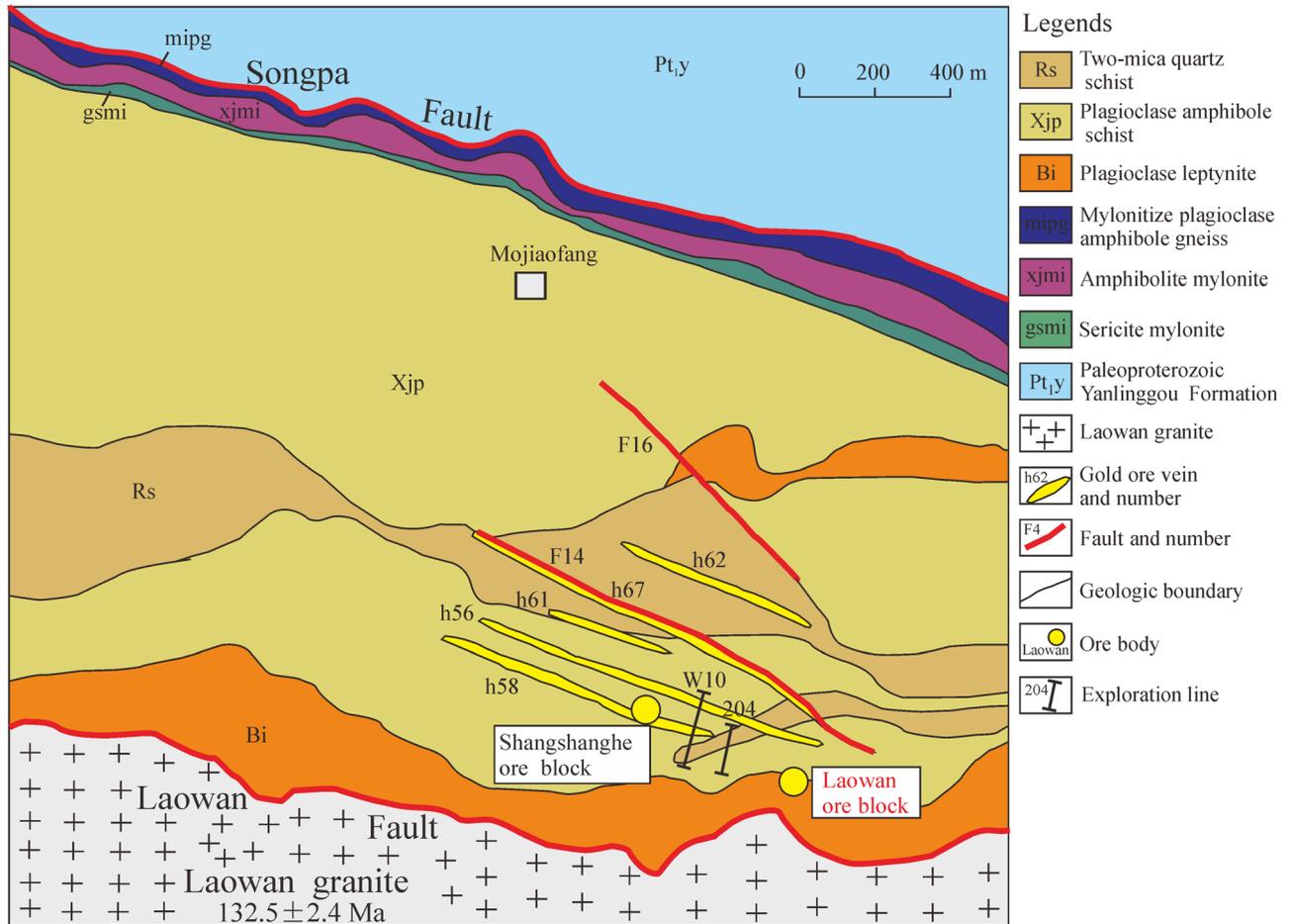
Fig. 2 Geological map of the Laowan gold deposit (modified after Kou et al., 2016).

deposit. The lengths are approximately 16 km, and the strikes are approximately 285° (Yang et al., 2015). The Laowan granite and Songpa granite porphyry dike intrude these faults, and also control the occurrence of ores and their secondary faults (Yang et al., 2014a and 2014b).

The magmatic activity in the study area was very strong and resulted in the formation of the Laowan granite, as well as its associated granite porphyry dikes and quartz porphyry dikes. The tabular Laowan granite is approximately 23 km long and 0.5 to 2 km wide (Yang et al., 2015). The Laowan intrusion is a biotite monzonite granite with a light pink color and porphyritic texture (zircon U-Pb age of 132.5±2.4 Ma; Liu et al., 2008a). Quartz albite porphyry dikes are widespread in the metallogenic belt and are less than 10 m in length. The alteration in the contact zones with these dikes is intense and associated with gold mineralization. The granite porphyry dikes (zircon U-Pb age of 139±3 Ma; Yang et al., 2015) occur in the northern region of the Laowan metallogenic belt and strike WNW. They are heavily fragmented at the edges of the veins, and Au-Ag polymetallic mineralization has been found in these zones.

The Laowan gold deposit is the primary mining area consisting of four nearly parallel gold veins. Most ore

bodies are hosted by the plagioclase amphibole schist and two-mica quartz schist. These ore bodies occur as stratiform, stratoid, lenticular, or vein bodies and are controlled by faults with steep dips of 60°–80° (Fig. 3).

The major ore minerals of the Laowan gold deposit include pyrite, chalcopyrite, and small amounts of native gold, electrum, galena, sphalerite, and arsenopyrite. The gangue minerals consist primarily of quartz, sericite, muscovite, and small amounts of epidote and zircon. Common ore textures include the automorphic/xenomorphic granular texture, cataclastic texture, poikilitic texture, solid solution structure, and metasomatic texture. The alteration types in the Laowan deposit include silicification, pyritization, K-feldspathization, sericitization, carbonatization, and epidotization. In addition, the boundaries between wall-rock alteration and mineralization are unclear, as gradual transitions are present. Gold mineralization is closely associated with silicification. Strong silicification leads to strong gold mineralization, while weak silicification leads to poor gold mineralization. Based on the observed field geological conditions, mineralogical assemblages, and crosscutting relationships, four stages of mineralization can be distinguished from early to late, as described below (Fig. 4).
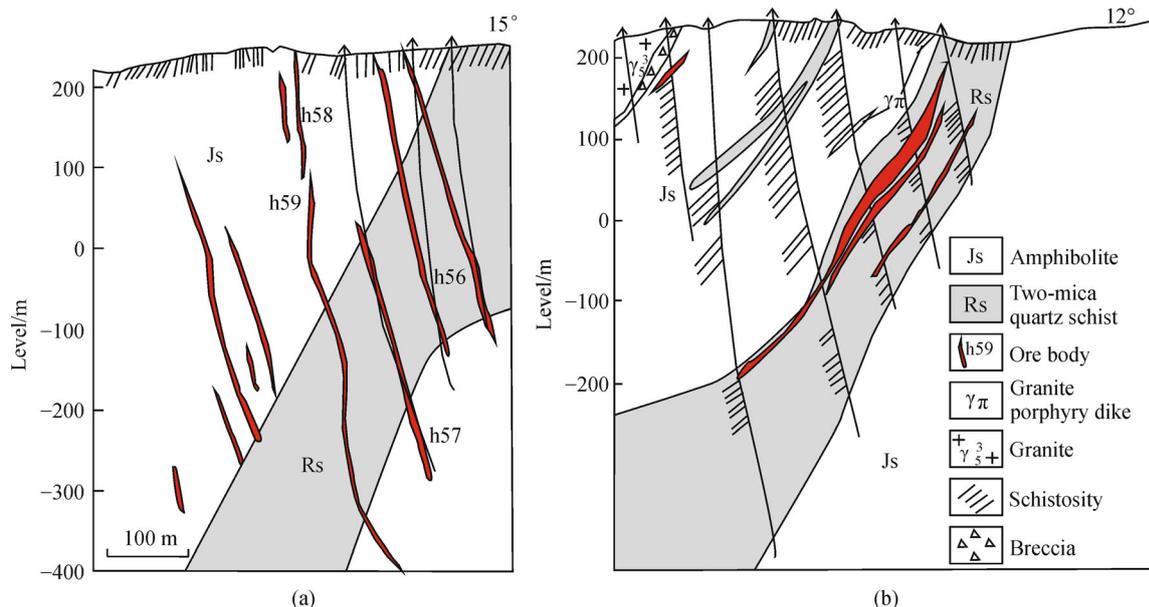
Fig. 3   Mineral geological map of (a) W10 exploration line and (b) 204 exploration line (after preliminary report of No. 1 Geological Exploration Institute Henan Bureau of Geo-exploration and Mineral Development).

Fig. 4   Stages of mineralization and mineral paragenesis in the Laowan gold deposit.

1) Stage I is primarily composed of milky, massive, and barren quartz and minor coarse-grained euhedral pyrite, which is labeled PyII (Figs. 5(d), 5(e), and 5(f)). The few pyrites are poorly developed and sporadically distributed in the quartz veins. The barren quartz and pyrite veins extend along strikes with cracks or are disseminated in the wall rock (Fig. 5(d)) and are commonly crosscut by later sulfide-bearing veinlets. In this stage, the Au mineralization is poor.

2) Stage II is defined by quartz, pyrite, and minor gold minerals. The quartz is smoky gray in color and darker than the earlier quartz, commonly displaying subhedral to euhedral features (Figs. 5(j) and 5(h)). Ubiquitous pyrite is present in the form of medium- to fine-grained subhedral-anhedral crystals, which occur as bands or veins parallel to the Stage I quartz veins (Fig. 5(h)). It generally forms disseminations coexisting with minor chalcopyrite in the quartz veins (Fig. 5(i)). This type of pyrite is denoted PyIII.

Chalcopyrite is intergrown with pyrite and quartz in irregular or stockwork forms or as inclusions in the pyrite (Figs. 5(i) and 5(k)). Minor anhedral pyrrhotite with a light rose color is also present, which encloses the earlier pyrite (Fig. 5(j)). Stage II is the early stage of Au mineralization. The gold minerals mainly include electrum (Fig. 5(k)) and minor native gold. The mineral assemblage observed in this stage is quartz + pyrite + native gold + electrum.

3) Stage III exhibits the major Au mineralization episode, characterized by abundant polymetallic sulfides, such as pyrite, chalcopyrite, galena, sphalerite, arsenopyrite, and native gold (Figs. 5(l), 5(m), 5(n), 5(o), and 5(p)). These sulfides occur in the form of disseminations or stockworks or are interspersed in fissures in the early pyrite, quartz, and other minerals (Figs. 5(n) and 5(p)). Pyrite occurs as euhedral-subhedral crystals bordered by chalcopyrite, pyrrhotite, or sphalerite (Figs. 5(n) and 5(o)). This type of pyrite is labeled PyIV. Chalcopyrite is intergrown with pyrite, sphalerite, quartz, and other minerals in irregular stockwork shapes or exists as inclusions in sphalerite (Fig. 5(n)). Sphalerite appears as irregular shapes that are intergrown with pyrite, galena, and chalcopyrite, and commonly contains pyrite and chalcopyrite inclusions (Figs. 5(n), 5(o), and 5(p)). A few examples of arsenopyrite can be found in SEM images. Most of the arsenopyrite is present in the form of silver-white, euhedral acicular, and prismatic crystals, with notably smaller sizes than those of the pyrites. Native gold exists as round inclusions in the sulfides or as irregular shapes distributed in the intergranular spaces or fissures in the sulfides. The mineral assemblage in this stage is quartz + pyrite + chalcopyrite + galena + sphalerite + native gold.
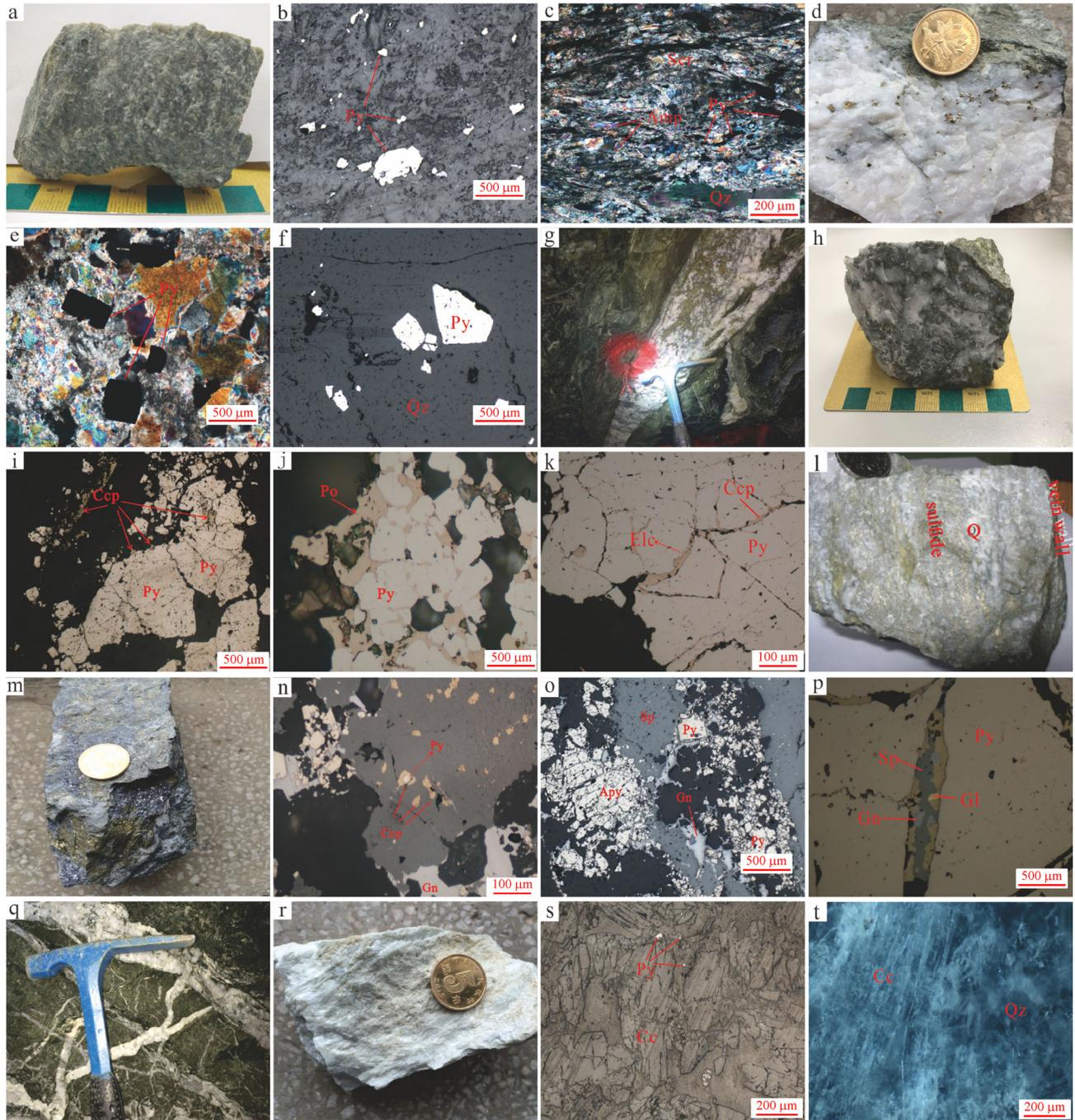
Fig. 5 Mineral assemblage characteristics of the Laowan gold deposit in different metallogenic stages. Metamorphic-diagenetic epoch: (a) plagioclase amphibole schist hand specimen (LW01); (b) irregularly shaped pyrites aggregates; (c) pyrites present mineral orientation. Mineralization Stage I: (d) milky, massive and barren quartz veins with little pyrite (LW02); (e) pyrites present star-like or spot-like distributions in milky quartz veins; (f) cubic pyrite crystals. Mineralization Stage II: (g) quartz vein, mainly consisting of quartz and fine-grained pyrite; (h) hand specimen of quartz and sulfides (LW03); (i) chalcopyrite in cracks or along the edges of pyrites; (j) anhedral pyrrhotite with a light rose color encloses the earlier pyrite; (k) chalcopyrite and electrum in the fissure of pyrite. Mineralization Stage III: (l) quartz vein (Stage II) coexisting with polymetallic sulfides (Stage III); (m) polymetallic sulfide ore hand specimen (LW04); (n) Pyrite is bordered by chalcopyrite, and chalcopyrite exists as inclusions in sphalerite; (o) sphalerite appears as irregular shapes and are intergrown with pyrite, galena and chalcopyrite and arsenopyrite; (p) chalcopyrite, galena, sphalerite and native gold are in the crack of pyrite. Mineralization Stage IV: (q) the early quartz veins (Stage I) cut by the latest barren calcite-quartz vein (Stage IV); (r) calcite hand specimen (LW05); (s) calcite with little pyrite; (t) calcite and quartz. Py-pyrite, Elc-electrum, Gn-galena, Sp-sphalerite, Ser-sericite, Qz-quartz, Gl-gold, Amp-amphibole, Apy-arsenopyrite, Ccp-chalcopyrite, Po-pyrrhotite, Cc-calcite.

4) Stage IV marks the waning of hydrothermal activity without any major metal deposition. This stage is characterized by the extensive formation of carbonate (calcite), some of which is interspersed within the early quartz veins (Figs. 5(q), 5(r), 5(s), and 5(t)). These veins are poorly developed and are distributed parallel to, perpendicular to, or at acute angles to the schistosity. Only a small quantity of anhedral pyrite is present (Fig. 5(s)) (called PyV); the mineral assemblage is calcite + quartz + pyrite.

3   Pyrite types and occurrence of gold

Based on the methods developed in previous studies of pyrites from sediment- and volcanic-hosted gold deposits (Mumin et al., 1994; Large et al., 2007 and 2009; Zhang et al., 2014), the morphologies and internal structures of pyrites are used here as indicators to establish the correlation between pyrite growth and gold mineralization.

A total of five hand specimens were collected from the ores, quartz veins, and wall rocks belonging to different stages and polished into sections for petrographic study. LW01, LW02, LW03, and LW04 were collected from exploration line 301, measurement point 5004, and LW05 was collected from exploration line 301, measurement point 1501. LW01 is a melanocratic plagioclase amphibole schist, which has columnar crystalloblastic fabric and block structure (Fig. 5(a)). The main minerals are plagioclase, amphibole, quartz, and minor sericite (Figs. 5(b) and 5(c)). LW02, LW03, LW04, and LW05 were collected from the four mineralization stages I, II, III, and IV, respectively. LW02 was collected from the barren quartz vein 100 m from LW01. The quartz vein is interspersed in the plagioclase amphibole schist. LW03 was collected near LW02. The sample is a quartz vein with abundant sulfides, mainly pyrite, chalcopyrite, and pyrrhotite, and minor electrum. LW04 was collected 300 m from LW03, which is near the fault. It is a massive ore with a high grade of Au. LW05 was collected from a carbonate-quartz vein.

Pyrite is widely developed in the study area and can be divided into five generations: one that formed during the metamorphic-diagenetic phase (PyI) and four that formed during the metallogenic phase (PyII, PyIII, PyIV, and PyV).

PyI occurs as euhedral-subhedral microcrystals with sizes of 5–10 μm (Fig. 5(b)) with irregularly shaped aggregates sized from 50–150 μm (Fig. 5(b)). PyI is preferentially hosted in the plagioclase amphibole schist and exhibits a mineral-parallel orientation (Fig. 5(c)). Hence, this generation of pyrite is considered to have formed during the metamorphic-diagenetic phase.

PyII occurs as euhedral crystals with large particle sizes (0.05–0.8 mm) and present as star- or spot-like distributions in milky quartz veins (Fig. 5(d)). Under the microscope, cubic pyrite crystals are predominant (Figs. 5(e), 5(f), and 5(g)); some pyrites have fissures at the edges that are filled with quartz veinlets. This generation of pyrite formed in the coarse-grained pyrite-quartz stage (Stage I). In this stage, the gold mineralization is poor, and minor Au exists dominantly in coarse-grained pyrite. Visible gold occurs in droplet-like and regular shapes with sizes of approximately 2 μm (Fig. 6(h)). This form of Au is regarded as electrum due to its high silver content (Figs. 7 (a) and 7(b)). The results of an energy spectrum analysis show that the Au is distributed throughout the pyrite and that the distribution of Ag is similar to that of Au (Fig. 7), indicating that the Au in PyII is mainly invisible gold (invisible solid solution or nanoparticles), with some visible electrum.

PyIII occurs as subhedral-anhedral crystals that are 0.05–0.5 mm in size (Figs. 5(i), 5(j), and 5(k)). Chalcopyrite is found in cracks or along the edges of this type of pyrite (Figs. 5(i) and 5(k)); some cubic crystals of pyrites are surrounded by pyrrhotite (Fig. 5(j)). Cracks are present within the pyrite and are often filled with quartz, chalcopyrite, galena, native gold, and electrum. This generation of pyrite formed in the quartz and the medium- to fine-grained pyrite stage (Stage II). This stage was the major metallogenic stage of the Laowan gold deposit. Numerous independent Au minerals (native gold and electrum) are visible under the microscope and in SEM images (Figs. 6(a), 6(b), 6(c), 8(a), 8(b), and 8(c)). Gold minerals with sizes of 1–10 μm form stockwork, veinlet, irregular granular, and oval patterns, and are primarily present within the pyrite and chalcopyrite particles, along crystal boundaries, and in cracks within the sulfides (Figs. 6(a), 8(a), and 8(c)). The microscopic and trace element characteristics of the gold minerals show that their silver contents are low; thus, they are native gold. The results of the energy spectrum analysis of the pyrite show that the distribution of Au is uniform (Fig. 8), which suggests the occurrence of invisible gold.

PyIV occurs as euhedral-subhedral crystals with sizes of 0.1–1 mm that are intergrown with chalcopyrite, galena, and sphalerite (Figs. 5(m) and 5(n)). The pyrite in this stage is highly fractured, and the cracks and edges of these pyrite grains are filled/coated with other sulfides (Fig. 5(o)). Arsenopyrite occurs in these cracks, as observed in the SEM images (Fig. 5(p)). This generation of pyrite formed in the polymetallic sulfide stage (Stage III). This was the most important stage of gold mineralization resulting in the formation of the highest-grade gold ore, which is currently the main focus of exploitation. Considerable microscopic particles of native gold were found along the boundaries between pyrite and chalcopyrite, and in cracks within the sulfides (Figs. 6(d), 6(e), and 6(f)). Thus, the gold minerals were observed to have formed after the sulfides, possibly via fluid metasomatism.
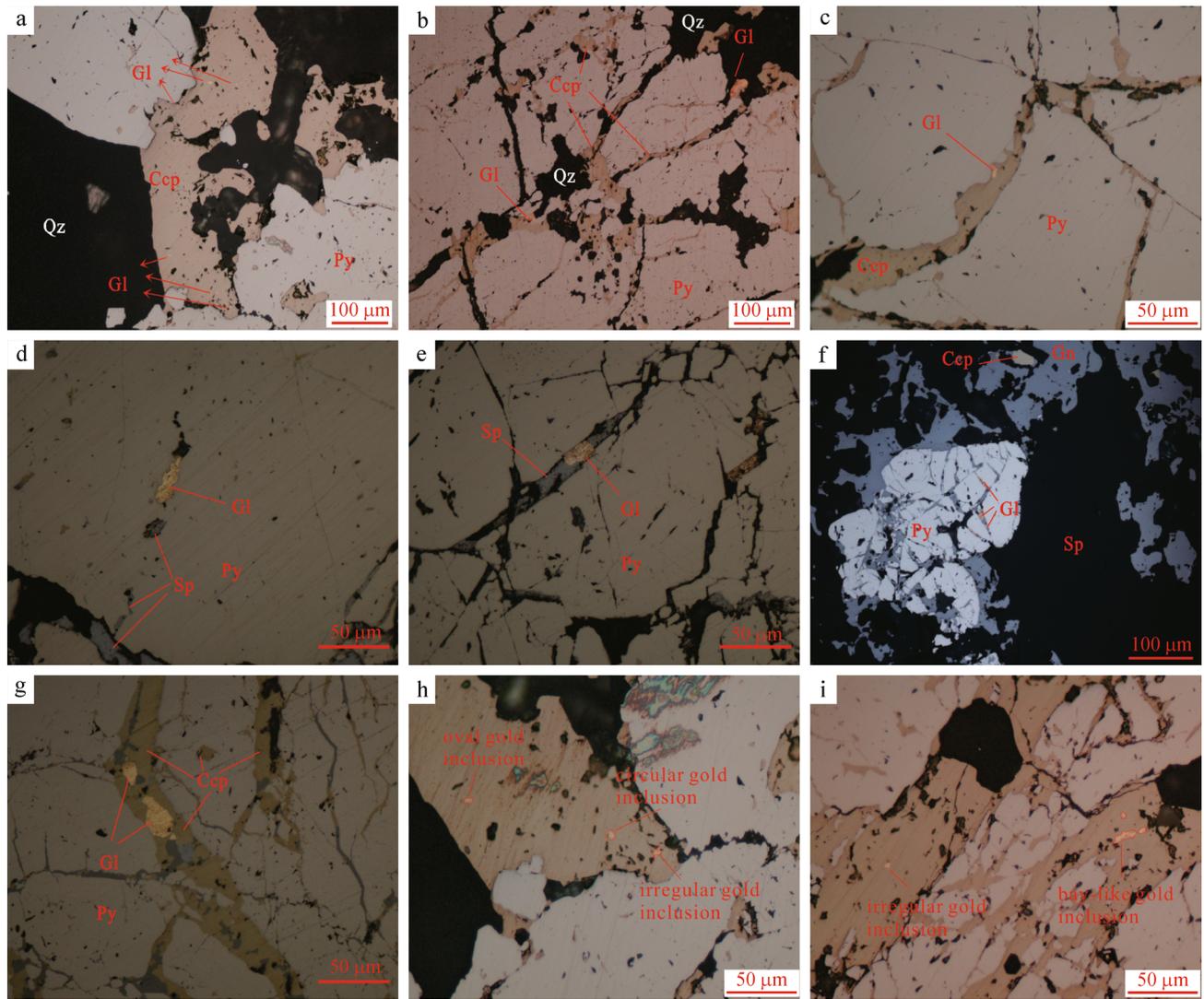
Fig. 6 The occurrence of visible gold. PyII: (h) oval gold inclusions in pyrite. PyIII: (a) gold inclusion in chalcopyrite; (b) and (c) gold inclusions in the boundaries of sulfides. PyIV: (d) gold in the fissure of pyrite; (e) and (f) gold in cracks of sulfides; (g) and (i) anhedral granular, acicular and flake gold inclusions. Gl – gold, Py – pyrite, Qz – quartz, Ccp – chalcopyrite, Gn – galena, Sp – sphalerite

The shapes and sizes of the gold minerals are diverse, but generally feature amorphous shapes, such as anhedral granular, acicular, and flake shapes (Figs. 6(g), and 6(i)). Additionally, single Au particles range from approximately 0.001 mm to 0.035 mm in size. The gold minerals are primarily native gold, and their Ag contents are lower than those observed in previous stages. The results of the energy spectrum analysis of the pyrite show similar distributions of Au and Ag (Fig. 9), but the concentration of Au is higher.

PyV occurs as euhedral-subhedral, predominantly cubic crystals, with sizes of 0.01–0.02 mm (Fig. 5(r)). This pyrite type is rare and is intergrown with calcite, dolomite, and quartz (Fig. 5(r)). This generation of pyrite formed in the carbonate-quartz stage (Stage IV), with no gold mineralization.

4 Analytical methods

4.1   LA-ICP-MS analysis of pyrite

The LA-ICP-MS analyses of pyrites were conducted on an Agilent 7700 Quadrupole ICP-MS instrument at the State Key Laboratory of Geological Processes and Mineral Resources, China University of Geosciences (Wuhan). This instrument was equipped with a 193 nm excimer laser ablation system (GeoLasPro). Helium was applied as a carrier gas. Argon was used as the make-up gas and mixed with the carrier gas via a T-connector before entering the ICP. A "wire" signal smoothing device is included in this laser ablation system (Hu et al., 2015). The spot size, frequency, and beam energy of the laser were set to 70 μm, 5 Hz, and ~5.5–6.5 J/cm^2, respectively. Trace element
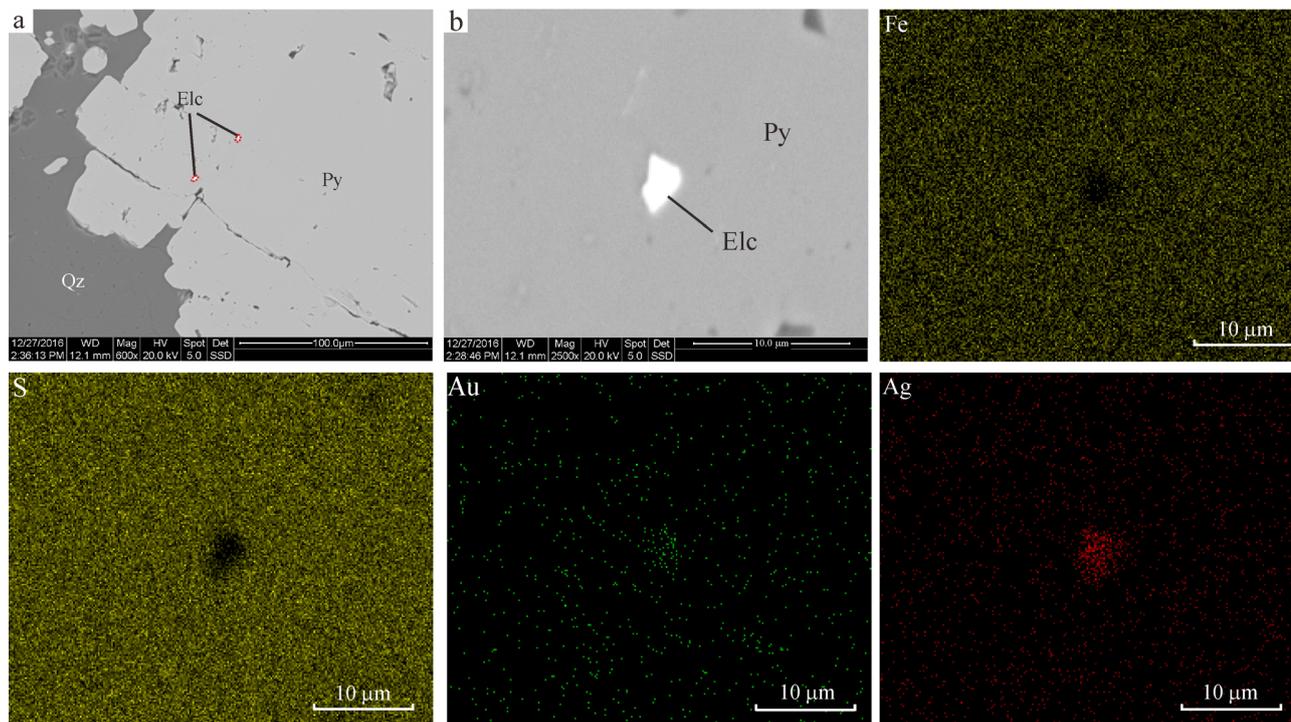
Fig. 7   SEM images of PyII. (a) and (b) electrum in PyII. Elc – electrum, Py – pyrite, Qz – quartz.

compositions of sulfides were calibrated against various reference materials (NIST 610 and NIST 612) without using an internal standard (Liu et al., 2008b). The sulfide reference material MASS-1 (USGS) was used as the unknown sample to verify the accuracy of the calibration method. Each analysis incorporated a background acquisition of approximately 20–30 s followed by 50 s of data acquisition from the sample. An Excel-based software ICPMSDataCal was used to perform off-line selection and integration of background and analyzed signals, time-drift correction, and quantitative calibration for trace element analysis (Liu et al., 2008b). A series of 55 elements were measured during each spot analysis (including S, Fe, Au, Ag, Cu, Pb, Zn, Co, Ni, Ge, As, Bi, Ti, Se, Sb, Al, Mg, Si, Cd, and rare earth elements (REEs)) in this study, but the concentrations of certain elements were below the detection limits.

4.2   *In situ* sulfur isotopes

The laser ablation multi-collector ICP-MS (LA-MC-ICP-MS) S isotope analyses of pyrites were carried out using a Neptune Plus MC-ICP-MS instrument coupled with a GeoLas 2005 excimer laser at the State Key Laboratory of Geological Processes and Mineral Resources, China University of Geosciences (Wuhan). Helium gas carrying an aerosol of each ablated sample was mixed with an argon carrier gas and nitrogen as an additional diatomic gas to enhance the sensitivity before finally flowing into the MC-ICP-MS instrument.

During the experiment, the diameter of the laser spot was 33 μm with a frequency of 10 Hz, the energy density was 2.7 J/cm^2, and the ablation process was set to last for 40 s. Standard sample bracketing (SSB) was used to determine the $\delta^{34}S$ values of the samples throughout the MC-ICP-MS analytical sessions. An international sphalerite standard NBS-123 ($\delta^{34}S_{V-CDT} = + 17.1$ ‰) and an in-house pyrite standard named WS-1, consisting of a natural pyrite crystal from the Wenshan polymetallic skarn deposit in Yunnan Province in south China, was used to calibrate the mass bias for S isotopes. The $\delta^{34}S_{V-CDT}$ values ($+ 1.1 \pm 0.2$ ‰) of WS-1 were determined with secondary ion mass spectrometry (SIMS) at the Chinese Academy of Geochemistry, Guangzhou (Zhu et al., 2016). The true sulfur isotope ratio of unknown samples was calculated with correction for instrumental mass bias by linear interpolation between the biases calculated from two neighboring standard analyses. The 2σ analytical precision was approximately ±0.3 per mil (Li et al., 2019).

4.3   H and O isotopes

In this paper, the H and O isotopes were determined on quartz and calcite grains obtained from the four stages of mineralization, but grains from the diagenetic stage were not analyzed. Pure quartz and calcite separates were prepared for the isotope analysis at the Analytical Laboratory Beijing Research Institute of Uranium Geology. The O isotope compositions of quartz and calcite were analyzed following the BrF$_5$ method (Clayton et al., 1972).
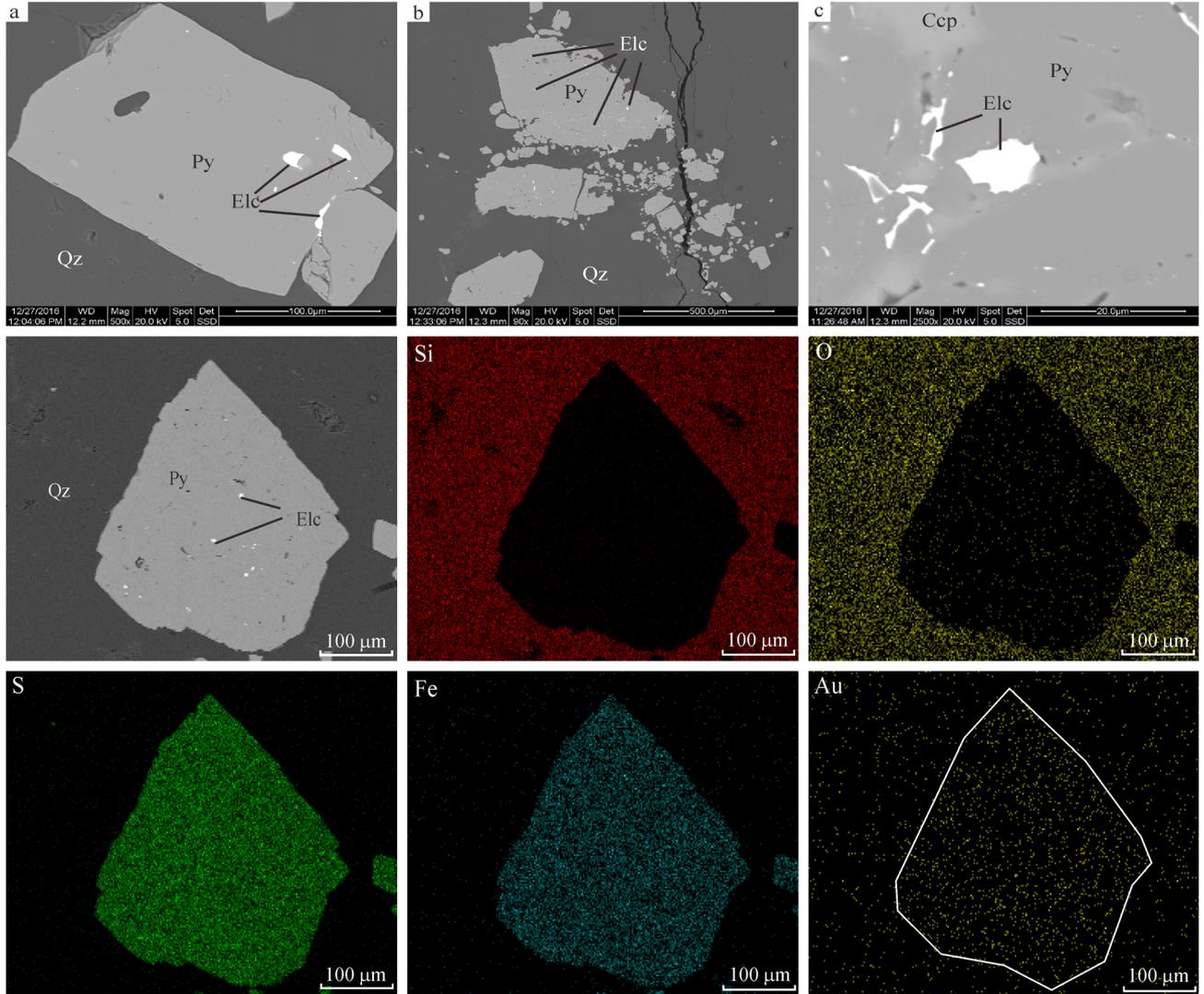
Fig. 8 SEM images of PyIII. (a), (b) and (c) irregular electrum in PyIII. Elc – electrum, Py – pyrite, Qz – quartz, Ccp – chalcopyrite.

The $\delta^{18}O$ values of these separates were determined on a Finnigan MAT 253 ratio mass spectrometer. The δD values of water were analyzed using the Zn reduction method (Coleman et al., 1982). H_2 and CH_4 from the fluid inclusions were first converted to H_2O by passing through a CuO furnace at a temperature of 600°C. Next, all of the H_2O was combined and converted to H_2 by reacting with Zn in a vacuum line. The δD values were measured on the same mass spectrometer. These results are reported relative to V-SMOW, and the analytical precisions are ± 0.2 ‰ for both $\delta^{18}O$ and δD. The degrees of isotopic fractionation between quartz and water and calcite and water were calculated using Eqs. (1) and (2) (Clayton et al., 1972) at the minimum trapping temperature, which was defined based on the average homogenization temperatures of the fluid inclusions in each quartz and calcite sample, as reported by Kou et al., (2016).

$$\delta^{18}O_{\text{water-SMOW}} = \delta^{18}O_{\text{V-SMOW}} - 10^3 \ln\alpha_{\text{quartz-water}}$$

$$= \delta^{18}O_{\text{V-SMOW}} - 3.38 \times 10^6/T^2 + 3.39, \qquad (1)$$

$$\delta^{18}O_{\text{water-SMOW}} = \delta^{18}O_{\text{V-SMOW}} - 10^3 \ln\alpha_{\text{calcite-water}}$$

$$= \delta^{18}O_{\text{V-SMOW}} - 2.78 \times 10^6/T^2 + 3.39. \qquad (2)$$

5 Results

5.1 LA-ICP-MS analysis of pyrite

A total of 35 LA-ICP-MS spot analyses were completed on pyrites selected from different samples from the Laowan deposit (Table 1), including 4, 8, 11, and 12 spots on PyI,
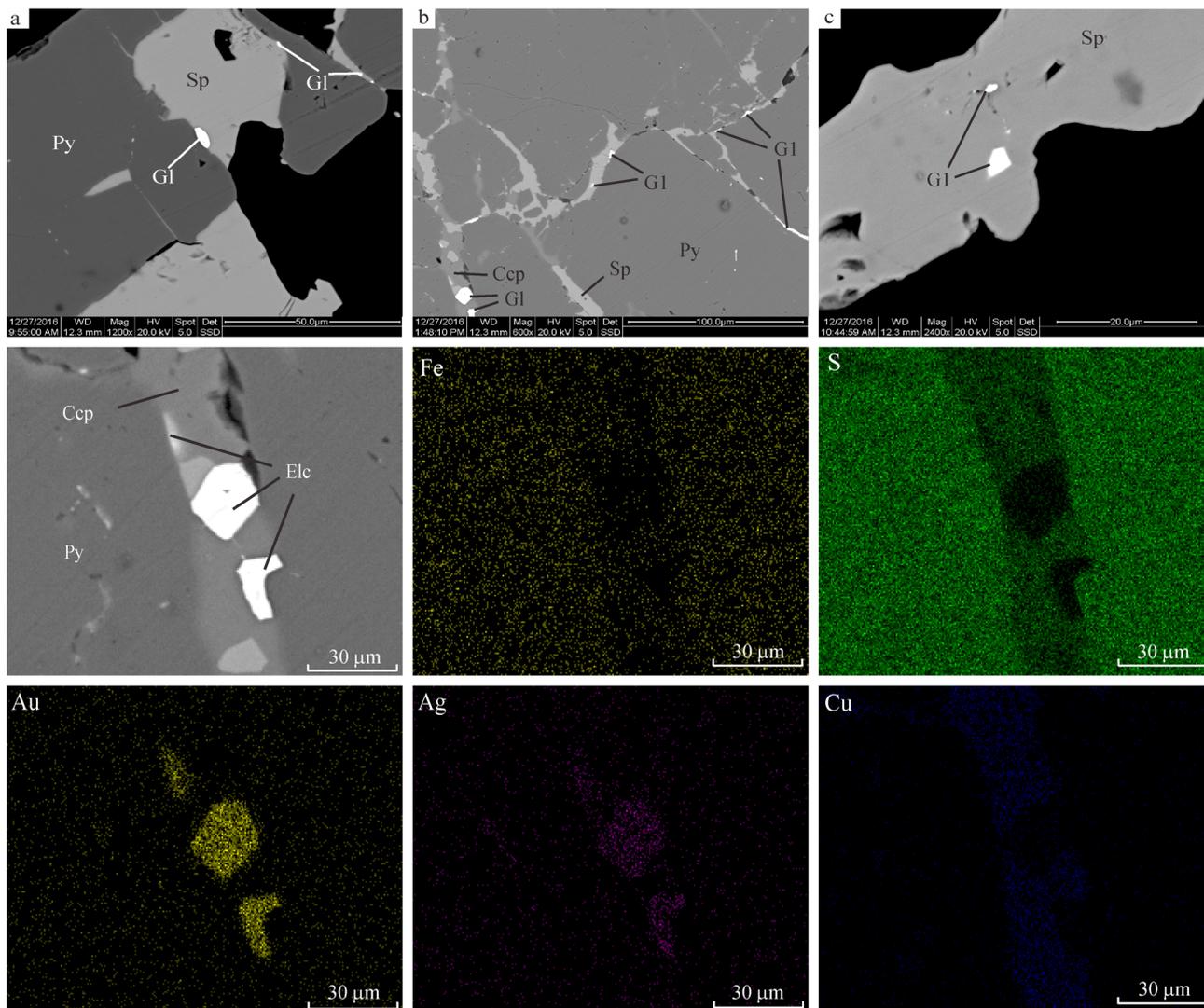
Fig. 9 SEM images of PyIV. (a), (b) and (c) gold inclusions in PyIII. Gl – gold, Sp – sphalerite, Elc – electrum, Py – pyrite, Qz – quartz, Ccp – chalcopyrite.

PyII, PyIII, and PyIV, respectively. PyV has no Au mineralization, and its size is too small to be analyzed by LA-ICP-MS; hence, it is not discussed further in this paper.

5.1.1 Characteristics of the LA-ICP-MS profiles of pyrite

To obtain precise trace element data from pyrite grains in this study, attempts were made to remove the larger inclusions (i.e., both fluid and some minor minerals). Distributions of the different trace elements in pyrite were estimated by LA-ICPMS analysis (Maslennikov et al., 2009; Zhang et al., 2014). Representative time-resolved depth profiles obtained from different generations of pyrite are illustrated in Fig. 10.

All spots on pyrites contain measurable quantities of gold. The concentration of Au in each sample is relatively constant, but varies in different samples by an order of

magnitude (Table 1). The time-resolved depth profiles of Au from PyIII and PyIV are wavy, with several spikes (Figs. 10(c) and 10(d)), suggesting the occurrence of Au inclusions in the pyrite. However, the Au distribution pattern for PyII is relatively flat (Fig. 10(b)), with no spikes, indicating that the Au primarily occurs as a solid solution or nanoparticles in the pyrite lattice (Cook et al., 2009; Zhang et al., 2014).

Silver is also an important trace element (Table 1). Figure 10 shows that the trend of Ag is parallel to that of Au, demonstrating that Ag may occur in the form of electrum. In PyII and PyIV, the trend of Ag is similar to that of Bi, which indicates that matildite likely occurs as a solid solution or as inclusions in the pyrite (Figs. 10(b) and 10(d)).

The time-resolved depth profiles for arsenic are flat, with no spikes (Fig. 10). As is abundant in these samples, thus

Table 1   LA-ICPMS analyses of selected pyrite grains from the Laowan gold deposit

Sample No.	Type	S	Fe	As	Au	Ag	Cu	Zn	Pb	Co	Ni	Ge	Bi	Ti
		/wt%	/wt%	/10^{-6}	/10^{-6}	/10^{-6}	/10^{-6}	/10^{-6}	/10^{-6}	/10^{-6}	/10^{-6}	/10^{-6}	/10^{-6}	/10^{-6}
LW01-1	PyI	47.71	51.66	2988	0.04	0.19	2.4	0.5	14.6	1275	430	11.9	0.33	628
LW01-2		47.47	51.8	2415	0.1	2.4	3.7	0.42	28.2	194	159	11.6	2.6	11.1
LW01-3		45.69	53.91	1470	0.97	13.8	4.2	0.57	36.4	499	665	12	3.6	12.7
LW01-4		42.62	57.03	1636	0.15	0.09	5.5	0.69	8	690	907	11.6	0.18	11.1
LW02-1	PyII	41.06	58.74	218	11.2	49	22.3	0.08	279	342	39.1	13.2	37.2	8.9
LW02-2		39.28	60.43	806	16.5	53.5	11.8	0.68	188	123	748	15.2	8.1	8
LW02-3		42.86	57.01	409	6	19.5	4.2	0.19	61.9	44	67	14.2	7.2	10.2
LW02-4		42.06	57.67	761	96.3	337	29.4	0.3	282	163	245	12.7	16.4	8.9
LW02-5		42.45	57.29	965	14.1	56.9	41.5	0.06	263	23.8	227	13.6	11.3	9.4
LW02-6		44.54	55.22	539	10.8	33.3	98.3	0.18	364	83.6	548	11.3	18.3	8.6
LW02-7		40.82	58.9	324	47.8	125	30.3	0.01	734	80.9	176	12.4	30.4	7.3
LW02-8		44.98	54.72	592	24.2	80.5	162	1	744	206	201	10.8	32	10
LW03-1	PyIII	47.38	52.21	2534	0.77	9.2	120	0	88.8	83	23.4	13.6	1.5	10.5
LW03-2		44.36	54.72	2270	1159	1952	2568	1.6	199	97.2	44.6	13.4	3.3	7.1
LW03-3		45.44	54.26	2181	0.16	0.56	2.8	0	12.9	43.2	28.5	12.5	0.07	8.1
LW03-4		46.68	53	2077	0.3	2.2	3.6	0.54	57.1	39.3	27.3	12	0.82	8.4
LW03-5		47.72	51.86	812	19.6	21	1911	1.2	205	1.1	8.8	11.6	3.6	9.4
LW03-6		48.68	51.11	956	0.31	1.5	3.2	0.46	46.5	8.8	35.2	13.3	0.81	7.9
LW03-7		51.56	47.75	511	4.9	80.1	3616	1.7	160	12.5	18.5	10.5	5.8	9.6
LW03-8		50.24	49.67	175	1.7	9.5	3.4	0.44	26.4	76.2	4	11.4	1.4	8.9
LW03-9		52.34	46.78	532	8.1	132	7129	4.6	213	32.9	28.7	11.3	9.9	10.4
LW03-10		50.97	48.86	543	6.6	27.5	2.4	0	47.7	9.3	26.5	11.1	4.1	5.3
LW03-11		51.93	47.89	619	9.9	38.1	32.1	0.12	150	87	37.6	11.8	9.8	8.4
LW04-1	PyIV	53.58	45.85	673	4.9	90	2313	1.1	390	16.8	328	10.7	6.3	25.8
LW04-2		56.67	43.07	327	7.3	65.8	93	0.2	589	35.4	236	10.5	6.3	7.2
LW04-3		53.02	46.65	989	20.8	182	96.8	0.27	464	83.8	890	10.6	2.4	6.9
LW04-4		56.15	43.56	912	22.5	155	139	1.2	239	77	356	10.9	3.1	7.5
LW04-5		55.49	41.89	2302	10.6	279	3044	622	15221	3.3	77.3	9.6	19.9	5.7
LW04-6.		57.56	40.57	1705	8.9	40.6	42.2	0.48	16392	0.98	41	11.2	16	6.5
LW04-7		55.64	43.9	1796	8.2	94.3	1116	0.84	603	0.4	34.9	10.9	2.8	8.2
LW04-8		59.97	39.79	980	2.5	14.6	33.8	0.13	124	25	297	10.1	1.1	8.5
LW04-9		57.92	41.77	2283	0.14	0.48	1.7	0	14.5	4.5	56.2	9.1	0.03	5.5
LW04-10		60.04	37.5	670	10.3	167	5437	14.9	16872	32.4	448	10	31.1	6.6
LW04-11		59.83	37.69	683	21.1	975	6715	1120	8797	164	305	9	48.3	3.8
LW04-12		60.48	38.65	188	4.1	42.9	807	2.4	5888	110	730	11.2	10.8	6

(*Continued*)

Sample No.	Type	Se /10^{-6}	Sb /10^{-6}	Co/Ni	Mg /10^{-6}	Al /10^{-6}	Cr /10^{-6}	Tl /10^{-6}	Mn /10^{-6}	Sn /10^{-6}	Ba /10^{-6}	V /10^{-6}	W /10^{-6}	Zr /10^{-6}
LW01-1	PyI	9.9	0.3	2.97	32	69.2	5.5	0	0.4	0.67	0.41	0.5	0.29	0.36
LW01-2		0	0.84	1.22	41	709	5.3	0.03	2.1	11.6	1.9	0.27	0	0.05
LW01-3		18.5	0.25	0.75	45.4	124	9.4	0.05	0.66	14.5	0.73	0.1	0.01	0.13
LW01-4		4.4	0.11	0.76	9.6	39.6	28.8	0	1.2	1.2	0.52	0.21	0.04	0.08
LW02-1	PyII	0	9.6	8.75	0.59	5.6	3.8	0.03	0.65	0	0	0.19	0	0
LW02-2		3.1	5.2	0.16	0.39	2	3.5	0.05	0	0	0.21	0.04	0	0.01
LW02-3		12.5	3	0.66	0.22	2.6	3.4	0.06	0	0	0.14	0.01	0	0.08
LW02-4		14.8	9.3	0.67	0.69	2.1	1.2	0.03	2.2	0.25	0.56	0.03	0.01	0
LW02-5		20.5	10.6	0.1	0.13	43.8	3.9	0.05	0.11	0.46	0.12	0.02	0.01	0.03
LW02-6		20.8	12.8	0.15	0.42	1.4	0.43	0.02	1.7	0.35	0.11	0	0	0.02
LW02-7		3.7	13.9	0.46	1.5	10.4	8	0.04	0.06	0.06	0.04	0	0.25	0
LW02-8		13.2	22	1.02	2.9	1.9	0.83	0.08	4.6	0.44	0.53	0	0.13	0
LW03-1	PyIII	29.8	6.2	3.55	0.32	0	1.6	0	0.83	0.22	1.1	0	0	0.01
LW03-2		21.7	12.2	2.18	1.5	15.7	3.4	0.05	0	0.15	0.11	0.02	0	0.3
LW03-3		20.1	0.39	1.52	0.77	1.3	5.4	0.01	1.3	0.1	0	0.07	0	0
LW03-4		6.7	3.1	1.44	0.48	1.8	4.3	0	0	0.29	0.18	0	0.02	0.06
LW03-5		6.1	13.5	0.13	0.66	1.4	6.2	0.04	0	0.24	0.16	0	0	0.04
LW03-6		17.3	3.2	0.25	0.31	1.5	2.7	0.01	0.59	0.45	0.07	0.04	0.01	0.06
LW03-7		0	11.4	0.68	0	1.7	1.2	0.06	16.4	0	0.27	0.09	0.02	0
LW03-8		27.2	1.4	19.05	0	0.28	9.2	0	26.7	0.32	0	0.02	0	0
LW03-9		26.9	16.7	1.15	0.59	0.71	0.22	0.05	33.3	0	0.05	0.02	0.01	0.01
LW03-10		18.3	2.5	0.35	0.63	0.72	0	0	0.68	0.09	0.04	0.1	0.01	0.01
LW03-11		7.2	6.4	2.31	0	1	1.3	0.04	0.27	0.18	0	0.06	0.03	0.03
LW04-1	PyIV	12.9	14.4	0.05	2	20.3	4.3	0.04	3.6	0.38	0.06	0.18	4.3	0.05
LW04-2		24.3	17	0.15	0.85	1.8	0.25	0.04	0	0.13	0.17	0.05	0	0.01
LW04-3		5.7	8.6	0.09	1.3	5.6	1.4	0.04	0.32	0	0.06	0	0	0.01
LW04-4		41.9	9.3	0.22	1.4	13.5	19.3	0.03	0.8	1.2	0.06	0.05	0	0.01
LW04-5		0	2883	0.04	0.05	0.13	0	0.14	52.9	0	0.28	0.04	0.02	0
LW04-6		11.1	20	0.02	1.2	4.2	0.64	0.03	0	1.1	0.03	0	0.01	0.01
LW04-7		35.1	10.6	0.01	0.24	1.9	4.5	0.01	0.44	0.18	0.06	0	0	0.02
LW04-8		16	4.6	0.08	0.4	0.16	1.9	0.02	0	0.07	0.06	0	0	0
LW04-9		0	0.66	0.08	0.82	0.25	0.87	0	0	0.23	0	0.06	0.03	0.02
LW04-10		20.5	88.4	0.07	0.41	0.05	0.81	0.09	1.7	0.63	0.04	0.04	0	0.02
LW04-11		1.8	4808	0.54	0.48	0.74	0	0.2	2.5	0.55	0.42	0	0	0
LW04-12		26.75	13.8	0.15	0.51	2.7	6.5	0.03	0	0.66	0.1	0.04	0.01	0.03
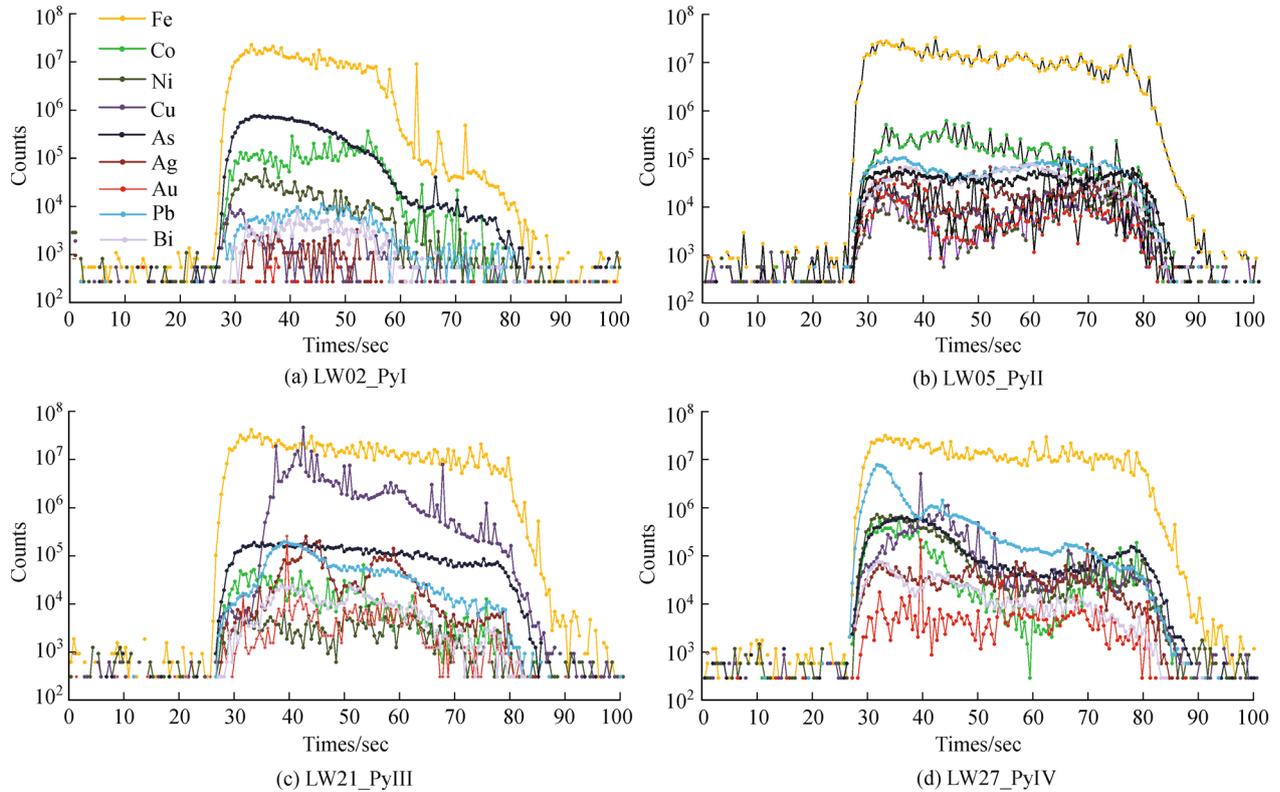
Fig. 10   Representative time-resolved depth profiles for pyrite analyzed in this study indicating the occurrences of gold and other major metal elements.

suggesting that the pyrites in the Laowan deposit bear As (Zhang et al., 2014) which is incorporated into the pyrite lattice.

The Pb concentrations vary over several orders of magnitude. The majority of higher concentrations (i.e., the spikes in Figs. 10(c) and 10(d)) can be readily attributed to inclusions of galena. However, in the samples of PyI and PyII, the consistent concentrations and flat time-resolved depth profiles (Figs. 10(a) and 10(b)) indicate the incorporation of Pb in solid solution into the pyrites.

Cobalt and Ni are common trace elements in pyrites, but the concentrations vary widely in different samples (Table 1). The flat and similar time-resolved depth profiles (Fig. 10(a)) observed of Co, Ni, and Fe demonstrate the presence of Co and Ni in the pyrite lattice.

Copper and Zn are also present in the pyrites, with higher concentrations of Cu than Zn (Table 1). The spikes of Cu in the time-resolved depth profiles indicate the presence of chalcopyrite inclusions.

5.1.2   Geochemical data of pyrite and their trends

Some of the elemental concentrations and their variations in the different types of pyrites are shown in Fig. 11.

The Au concentrations in PyI, PyII, PyIII, and PyIV are 0.04–0.15×10^{-6}, 6.0–96.3×10^{-6}, 0.16–19.3×10^{-6}, and 0.14–22.5×10^{-6}, respectively (Table 1, Fig. 11(a)). The Ag

concentrations are 0.09–13.8×10^{-6}, 19.5–337×10^{-6}, 0.56–132×10^{-6} (with a maximum value of 1952×10^{-6}), and 0.48–975×10^{-6}, respectively (Table 1). The samples from the metallogenic epoch (PyII, PyIII, and PyIV) have higher concentrations of Au and Ag than PyI samples (Fig. 11(a)). The Ag-Au plot shows a prominent positive correlation between Au and Ag, indicating that some Ag occurs as electrum. As confirmed by the results of the energy spectrum analysis and microscopic observations, abundant Au and Ag occur as visible native gold and electrum within pyrite crystals and fissures, as well as in sulfide cracks. Furthermore, the results of energy spectrum analyses and the relatively parallel smooth time-resolved depth profiles of Au and Ag show that some Au and Ag are homogeneously distributed within the pyrite as an invisible solid solution or nanoparticles in the pyrite crystal lattice. The Pb vs. Ag and Sb vs. Ag plots show positive correlations of Ag with Pb and Sb, indicating that Ag may occur as a S-Sb compound (e.g., argyrythrose) in galena (Cook et al., 1998; Zhang et al., 2014)

The arsenic concentrations range from 175 to 2988×10^{-6}. The generally flat LA-ICP-MS time-resolved depth profiles for As indicate that As occurs in the different types of pyrite via isomorphism (Table 1). Small amounts of Au are incorporated into the pyrite lattice or the interstices when some elements (e.g., As, Te, and Sb) distort the pyrite lattice (Palenik et al., 2004; Reich et al.,
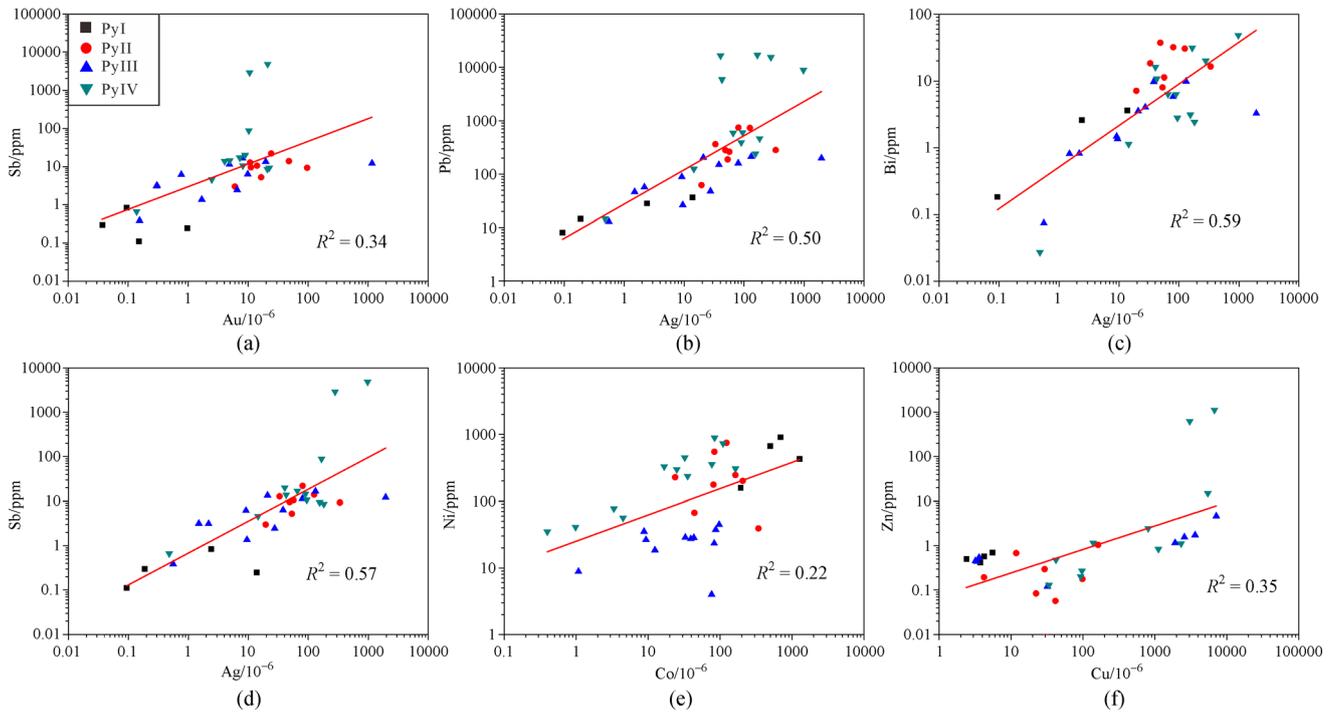
Fig. 11 Binary plots of (a) Ag vs. Au, (b) As vs. Au, (c) Bi vs. Au, (d) Ni vs. Au, (e) Pb vs. Au, (f) Cu vs. Au, (g) Sb vs. Au, (h) Pb vs. Ag, (i) Bi vs. Ag, (j) Sb vs. Ag, (k) Ni vs. Co, (l) Zn vs. Cu in different pyrite types. The trace element concentrations are from Table 1.

2005 and 2006; Cook et al., 2009; Zhao et al., 2011). However, the As-Au plot shows that in PyII, PyIII, and PyIV, no correlation exists between As and Au (Fig. 11(b)), indicating that the enrichment of Au in the Laowan gold deposit is unrelated to As. This may be due to the presence of gold in the Laowan gold deposit is mainly visible gold, and does not become incorporated into the pyrite lattice.

Both Co and Ni are abundant in pyrite and enter the lattice via the isomorphous replacement of Fe (Zhang et al., 2014), and their concentrations are $0.40–1275 \times 10^{-6}$ and $4.0–907 \times 10^{-6}$, respectively. The Co-Ni plot reveals that Co and Ni have a certain positive correlation (Fig. 11(k)). On the Co/Ni-Au/Ag plot (Fig. 12), the PyI spots plot close to Co/Ni = 1, and the PyII and PyIV spots primarily plot in the third quadrant with Co/Ni < 1. The PyIII spots plot in the second and third quadrants with values of Co/Ni > 1 and Au/Ag < 1. Because Co is incorporated into the pyrite lattice, the good positive correlations observed between Pb/Co and Au/Co, and between Ag/Co and Bi/Co, may also indicate that these elements (Pb, Au, Ag, and Bi) typically occur as discrete, minute inclusions in pyrite (Fig. 13) (Zhao et al., 2011).

Compared with the pyrite that formed during the metallogenic period (PyII, PyIII, and PyIV), the diagenetic pyrite (PyI) contains lower concentrations of Cu and Zn (Table 1). The Zn-Cu plot shows a positive correlation, indicating the coexistence of chalcopyrite and galena inclusions (Fig. 11).
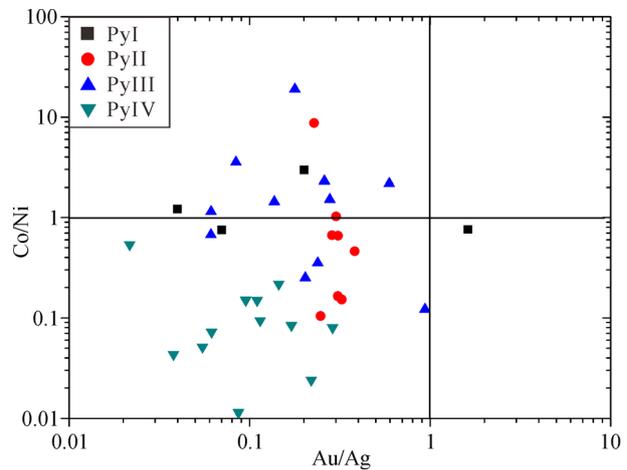
Fig. 12 Binary plots of Co/Ni vs. Au/Ag.

Lead is least likely to be incorporated into the pyrite crystal lattice due to its ionic size. Pb forms galena prior to forming pyrite (Huerta-Diaz and Morse, 1992; Morse and Luther, 1999; Koglin et al., 2010), and galena inclusions in pyrite are common (Zhao et al., 2011). The high concentration of Pb observed in PyIV supports this hypothesis.

5.2 Sulfur isotopes

The S isotope results obtained from the present study and
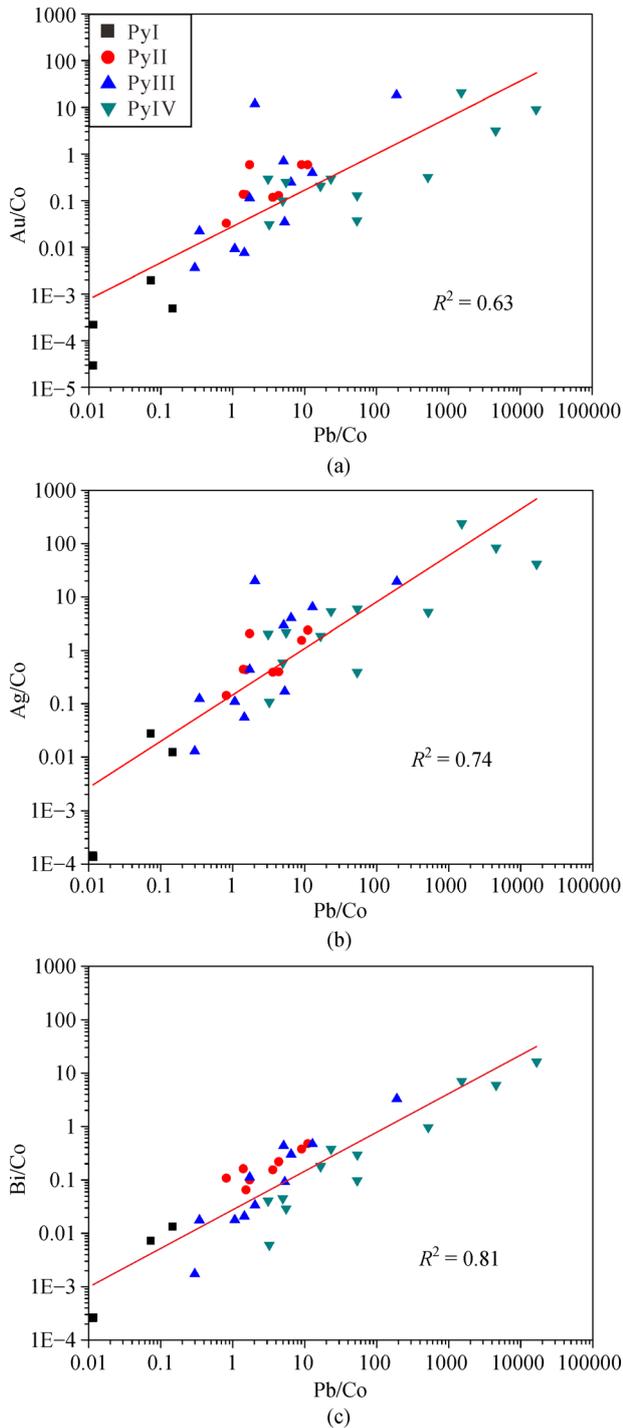
Fig. 13 Correlation diagrams of Pb/Co and Au/Co, Ag/Co and Bi/Co ratios for all the LA-ICP-MS analyses showing good correlations. Correlation coefficients (R) are given in the figures.

previously published studies are presented in Table 2 and Table 3, respectively. The measured δ^{34}S values of the four stages of pyrites range from 1.45 ‰ to 5.55 ‰ ($n = 15$, average = 3.89 ‰) (Table 3), while the S isotope compositions of the ores show a tower distribution. From PyI to Py III, the sulfur isotopes obviously increase, and

subsequently, the sulfur isotope of PyIV decreases (Fig. 14). PyI has the lowest δ^{34}S values, ranging from 1.45 ‰ to 2.09 ‰, with an average of 1.77 ‰. The δ^{34}S values of PyII, PyIII, and PyIV range from 3.10 ‰–4.21 ‰ (average = 3.55 ‰), 4.44 ‰–5.55 ‰ (average = 5.16 ‰), and 3.87 ‰–4.12 ‰ (average = 3.75 ‰), respectively. Based on these S isotope data, we can conclude that the diagenetic fluid and ore-forming fluids have different sulfur sources. The δ^{34}S values of pyrite reflect the H_2S in the fluid that precipitated the pyrite. Given sulfides are the most abundant sulfur-bearing minerals in the Laowan gold deposit,, with pyrite being dominant, the small proportions of other sulfides have minor effects on the total sulfur signature of the hydrothermal fluid (Dong et al., 2018). Hence, the δ^{34}S value of pyrite and the primary δ^{34}S value of H_2S in the hydrothermal fluid should be related as shown in Eq. (3) (Ohmoto and Goldhaber, 1997).

$$1000\ln\alpha_{pyrite\text{-}H_2S} = 0.4 \times 10^6/T^2 = \delta pyrite - \delta H_2S. \quad (3)$$

The calculated δ^{34}S values of the ore-forming fluids are 2.03 ‰–3.14 ‰ in Stage I, 3.00 ‰–4.12 ‰ in Stage II, and 2.26 ‰–2.51 ‰ in Stage III, based on the fluid inclusion average homogenization temperatures of 337°C, 256°C, and 225°C, respectively (Kou et al., 2016; Table 3).

5.3   Hydrogen and oxygen isotopes

The fluid inclusions in the quartz and calcite samples studied here show δD values ranging from -76.8 ‰ to -108.9 ‰. The four stages of mineralization show a systematic decrease in the δD values: the δD values of the four samples overlap, ranging from -77.4 ‰ to -76.8 ‰ in Stage I, -85.6 ‰ to -79.4 ‰ in Stage II, -90 ‰ to -77.8 ‰ in Stage III, and -108.9 ‰ to -96.5 ‰ in Stage IV. The quartz and calcite samples from these four stages of mineralization show δ^{18}O values ranging from 10.2 ‰ to 11.8 ‰ (Table 4), exhibiting a gradual decrease that is not obvious. The δ^{18}O values of the samples are 10.9 ‰–11.8 ‰ in Stage I, 10.8 ‰–11.8 ‰ in Stage II, 0.8 ‰–11.5 ‰ in Stage III, and 10.2 ‰–11 ‰ in Stage IV. Calculating the precise $\delta^{18}O_{H_2O}$ values of the fluids that were in equilibrium with the quartz and calcite is difficult due to the large variation in the temperatures obtained from the fluid inclusions (Goldfarb et al., 2004). Here, we use the average homogenization temperatures of these fluid inclusions to calculate their $\delta^{18}O_{H_2O}$ values. The average homogenization temperatures (Kou et al., 2016) of the fluid inclusions obtained from each of the quartz samples are listed in Table 4. The calculated $\delta^{18}O_{H_2O}$ values of these fluids are similar in all four samples and show a systematic decrease with the evolution of the mineralization stages. The $\delta^{18}O_{H_2O}$ values of the samples are 5.2 ‰–6.1 ‰ (average = 5.7 ‰) in Stage I, 2.7 ‰–3.1 ‰ (average = 2.7 ‰) in Stage II, 0.6 ‰–1.3 ‰ (average = 1.0 ‰) in

Table 2 Previous studies of $\delta^{34}S$ isotope characteristics in the Laowan gold deposit

Objects	Samples	$\delta^{34}S/‰$ (n)	Reference
Ore	Pyrite	1.4–3.8 (4)	Chen (2017)
Guishanyan Formation	Whole rock	2.5 (1)	
Laowan Granite	Whole rock	3.7 (1)	
Ore	Pyrite	2.9–5.8 (17)	
Ore	Galena	1.9–4.4 (3)	
Ore	Sphalerite	3.3 (1)	
Ore	Chalcopyrite	4.9 (1)	
Guishanyan Formation	Pyrite	3.6–4.3 (5)	
Ore	Pyrite	2.9–6.0 (21)	He and Wang (2005)
Ore	Galena	1.69–2.69 (3)	
Ore	Sphalerite	3.33 (1)	
Ore	Chalcopyrite	4.9 (1)	
Guishanyan Formation	Pyrite	3.63–4.26 (5)	
Guishanyan Formation	Galena	2.78 (1)	
Alterated rocks-quartz vein	Pyrite	2.9–5.9 (29)	Yang et al. (2014b)
	Galena	1.7–2.8 (4)	
	Sphalerite	3.3 (1)	
	Chalcopyrite	4.9 (1)	

Table 3 $\delta^{34}S$ isotope characteristics of pyrites and fluid in the Laowan gold deposit

	Sample	$\delta^{34}S_{pyrite}/‰$	$T/°C$	$\delta^{34}S_{H_2S}/‰$
Ore	Pyrite (PyI)	1.45	/	/
		2.09	/	/
	Pyrite (PyII)	3.49	337	2.42
		3.40	337	2.33
		3.10	337	2.03
		4.21	337	3.14
	Pyrite (PyIII)	5.17	256	3.74
		5.48	256	4.05
		4.43	256	3.00
		5.55	256	4.12
	Pyrite (PyIV)	4.12	225	2.51
		3.87	225	2.26
		4.04	225	2.43
		3.95	225	2.34
		4.02	225	2.41

Note: $\delta^{34}S_{H_2S}/‰$ represent the $\delta^{34}S$ of hydrothermal fluid that precipitated the pyrite.

Stage III, and $-1.7‰–-0.9‰$ (average $= -1.3‰$) in Stage IV.
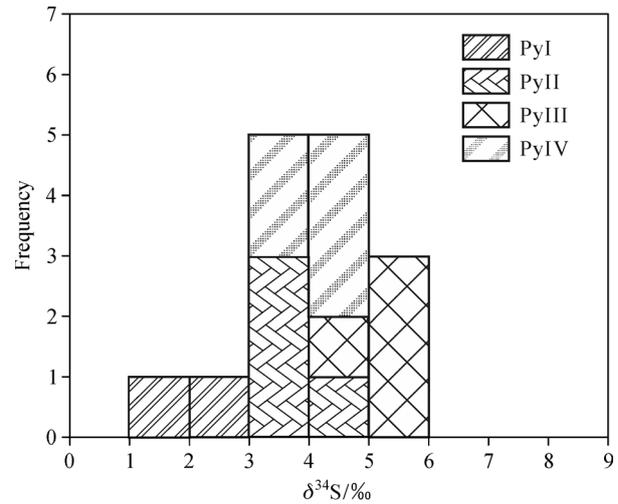
Fig. 14 $\delta^{34}S$ of the pyrites in Laowan gold deposit.

6 Discussion

6.1 Sources of ore-forming fluids

The δD values obtained from fluid inclusions in quartz and calcite can accurately reflect the δD values of the original hydrothermal fluids (Faure, 2003; Yan et al., 2014). The δD values observed here show a systematic decrease through the four stages of mineralization, decreasing from $-77.1‰$ to $-82.8‰$, $-84.7‰$, and $-102.7‰$ (Table 4). The $\delta^{18}O$ values of quartz and calcite are indistinguishable and fall in a narrow range of 10.2‰–11.8‰ (Table 4). The $\delta^{18}O_{H_2O}$ values that were calculated using the formula based on the $\delta^{18}O$ values of quartz and calcite can represent the $\delta^{18}O$ values of the ore-forming fluid. In Table 4, the values of $\delta^{18}O_{H_2O}$ also exhibit a gradual decrease with the evolution of mineralization. On the plot of δD vs. $\delta^{18}O_{H_2O}$ (Fig. 15), all the samples in the Laowan gold deposit are located between the magmatic water field and the meteoric water line. These hydrogen and oxygen isotope data deviate from the values of magmatic water ($\delta D = -80‰–-40‰$, $\delta^{18}O_{H_2O} = 5.5‰–9.5‰$), proposed by Ohmoto (1986) and Sheppard (1986). As shown in Fig. 15, the fluids of the Laowan gold deposit may represent magmatic water mixed with some meteoric water: in Stage I, the ore-forming fluids were primarily derived from magma; in Stages II and III, some meteoric water was added into these fluids, thus increasing its proportion; and in Stage IV, the ore-forming fluid was mainly meteoric water.

6.2 Sources of sulfur

Under equilibrium conditions, the enrichment sequence of S in sulfides is $Bi_2S_3 < Sb_2S_3 < Cu_2S < PbS < Cu_5FeS_4 < CuFeS_2 < ZnS < FeS_{1-X} < FeS_2 < MoS_2$. The sulfides in

Table 4 H and O isotope characteristics of different stages of mineralization in the Laowan gold deposit

Sample No.	Mineral	Stages of mineralization	Homogenization temperature*/°C	$\delta^{18}O_{mineral}$/‰	$\delta^{18}O_{H_2O}$/‰	δD_{H_2O}/‰
LWB-1-2	quartz	I	337	11.8	6.1	−76.8
LWB-1-4	quartz			10.9	5.2	−77.4
Average				11.35	5.65	−77.1
LWB-2-1	quartz	II	256	11	2.3	−85.6
LWB-2-5	quartz			11.8	3.1	−83
LWB-2-6	quartz			10.8	2.1	−79.4
LWB-2-11	quartz			11.8	3.1	−83.2
Average				11.35	2.65	−82.8
LWB-3-1	quartz	III	225	10.8	0.6	−77.8
LWB-3-2	quartz			11.5	1.3	−86.3
LWB-3-3	quartz			11.4	1.2	−90
Average				11.23	1.03	−84.7
LWB-4-1	calcite	IV	153	11	−0.9	−108.9
LWB-4-2	calcite			10.2	−1.7	−96.5
Average				10.6	−1.3	−102.7

Note: * The data of homogenization temperatures of fluid inclusions were from Kou et al. (2016).
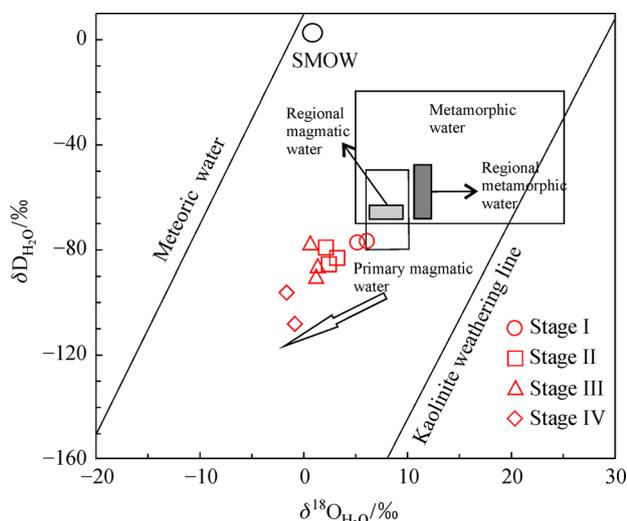
Fig. 15 Plot of δD versus $\delta^{18}O_{H_2O}$ for ore-forming fluids of the Laowan gold deposit (modified by Taylor, 1997). SMOW: standard mean ocean water.

the different mineralization stages of the Laowan gold deposit are present in the following order: $\delta^{34}S$ (pyrite) > $\delta^{34}S$ (sphalerite) > $\delta^{34}S$ (galena) (Table 2), indicating that the various minerals in the ore-forming fluid reached S isotope equilibrium. Because pyrite is the main sulfide, the small proportions of other sulfides have minor effects on the total sulfur signature of the hydrothermal fluids, and the S isotope composition of pyrite thus approximately represents the S isotope composition of the ore-forming fluid (Zheng and Chen, 2000).

In this paper, the $\delta^{34}S$ values of the pyrites range from 1.45 ‰ to 5.55 ‰, and the $\delta^{34}S$ values of PyI (1.45 ‰– 2.09 ‰) are close to zero, similar to those of meteorite S (0±3 ‰). These values are obviously lower than those of the metallogenic pyrites, indicating that the hydrothermal fluids present during diagenesis were different from the ore-forming fluids present during mineralization. Previous studies have shown that the $\delta^{34}S$ values of the whole-rock Guishanyan Formation, the pyrite from the Guishanyan Formation, and the whole-rock Laowan granite are 2.5 ‰, 3.6 ‰–4.3 ‰, and 3.7 ‰, respectively (He and Wang, 2005; Ding and Wang, 2014; Yang et al., 2014b; Chen 2017), which are similar to the $\delta^{34}S$ values of the samples. The $\delta^{34}S$ values of PyI are similar to those of the whole-rock Guishanyan Formation, indicating that its source of sulfur may be consistent with the source of the protolith of plagioclase amphibole schist. The $\delta^{34}S$ values of PyII, which are lower than those of pyrites from the other two stages of mineralization, are similar to the values of the Guishanyan Formation, showing that its S is mainly derived from strata. A mathematical mixing model is used to process the S compositional data from the samples (Li, 2007) and shows that the S in the Laowan gold deposit was derived from two sources: 41% from the Laowan granite, and 59% from the Guishanyan Formation. Therefore, we conclude that the S in the ore-forming fluids was derived from both strata and the Laowan granite.

6.3 Pyrite genesis

The concentrations of Co and Ni in pyrite can reflect the origin of the pyrite and the geological setting in which it

was formed (Bralia et al., 1979; Cook et al., 2009). Nickel can be easily incorporated into the pyrite crystal lattice via isomorphous replacement of Fe and is not readily released during the hydrothermal recrystallization (Huerta-Diaz and Morse, 1992; Morse and Luther, 1999; Tribovillard et al., 2006; Large et al., 2009; Koglin et al., 2010; Zhao et al., 2011). Ultramafic and certain mafic rocks are typically strongly enriched in Ni; in contrast, felsic rocks usually contain low Ni concentrations. Consequently, the pyrite grains from granite-related gold deposits are expected to contain negligible Ni (Zhao et al., 2011). In the Laowan gold deposit, the Ni concentrations are highest in PyI, demonstrating that in the diagenetic stage, the ore-forming fluid was primarily derived from the Guishanyan Formation, which has relatively high Ni concentrations because its protoliths were intermediate to basic volcanic rocks and clastic rocks. The Ni concentrations of PyII, PyIII, and PyIV are obviously lower than those of PyI, which may be due to the ore-forming fluids originated from the Laowan granite and meteoric water in the metallogenic stage. In addition, PyIII and PyIV are intergrown with abundant chalcopyrite and galena, indicating that the physicochemical conditions and composition of the ore-forming fluid changed considerably, and that more Cu and Pb had been leached into the ore-forming fluid. Previous studies have also shown that pyrites related to magmatic or volcanic hydrothermal fluids have Co/Ni values > 1 and that their concentrations of Co and Ni vary greatly. In contrast, pyrites that underwent sedimentary genesis typically exhibit Co/Ni values that are smaller than 1 with lower concentrations of Co and Ni (Loftus-Hills and Solomon, 1967; Price, 1972; Bralia et al., 1979). Nonetheless, when using the Co/Ni ratio to classify and discriminate, the context of geological evidence should be considered because numerous hydrothermal pyrites have Co/Ni ratios less than 1.0 (Price, 1972; Bralia et al., 1979). The concentrations of Co and Ni are highest in PyI, with the Co/Ni ratios ranging from 0.75 to 2.97, with an average of 1.42 (Table 1). However, the S isotope composition (1.45 ‰ to 2.09 ‰) of PyI indicates that the S derived from the Guishanyan Formation. So, we consider that PyI is metamorphic hydrothermal origin. The concentrations of Co and Ni in PyII are lower, with Co/Ni ratios ranging from 0.10–1.03 (with an average of 0.46). However, the PyII formed in Stage I has positive $\delta^{34}S$ values (ranging from 3.10 to 4.21 ‰, mean 3.55 ‰), which are closely associated with magmatic-hydrothermal activity. Therefore, PyII should be classified as magmatic in origin. The concentration of invisible gold is highest in PyII, which corresponds to the initial Au enrichment stage. Compared with PyII, PyIII contains lower concentrations of Co and Ni, with Co/Ni values ranging from 0.12 to 3.55 (with an outlier of 19.07 and an average of 1.35). The range of Co/Ni values increases, which is characteristic of the addition of magmatic hydrothermal fluids (Table 1). The invisible gold concentration decreased significantly, while the

concentration of visible gold increased, indicating that the invisible gold in pyrite was extracted by the added magmatic hydrothermal fluid and the resulting Au-bearing fluid precipitated Au in the fissures in pyrite and cracks in sulfides. Compared with other types of pyrites, PyIV has lower Co and higher Ni concentrations, with Co/Ni ratios of 0.01–0.54 (with an average of 0.13); the $\delta^{34}S$ values of PyIV (range from 3.87 ‰ to 4.12 ‰) are closely associated with magmatic hydrothermal activity. In this stage, numerous other sulfide minerals formed, which may have occurred because a larger amount of meteoric water was added during this mineralization stage , and the changes in temperature and pressure might have caused more Cu, Zn, and Pb to precipitate from the ore-forming fluid (Zhao et al., 2011; Hu et al., 2019). In addition, this pyrite phase is especially enriched in microscale Au.

Due to the similar geochemical characteristics of Se and S, Se can partially replace S in pyrite. This isomorphism is much more favorable under conditions of endogenous hydrothermal mineralization than it is under those of exogenous deposition (Song, 1984; Song and Zhang, 1986). Previous studies have shown that the Se concentrations of pyrites that form from sedimentogenesis are 0.5×10^{-6}–2×10^{-6} and that their S/Se ratios can reach up to tens or hundreds of thousands. In contrast, the Se concentrations of pyrites related to magmatic hydrothermal fluids are greater than 20×10^{-6}, and their S/Se values are smaller, generally less than 15000 (Liu et al., 1984; Song, 1984; Zhou et al., 2010; Xing et al., 2016). The Se concentrations of the pyrites from the Laowan gold deposit are 0–42.0×10^{-6} (with an average of 14.3×10^{-6}), yet most greater than 2×10^{-6}. The Se concentrations in PyI, PyII, PyIII, and PyIV are 0–18.5×10^{-6}, 0–20.8×10^{-6}, 0–29.8×10^{-6}, and 0–41.9×10^{-6}, respectively. The Se contents of PyIII and PyIV are higher than those of PyI and PyII. Therefore, we suggest that the addition of magmatic hydrothermal fluid may have occurred during the formation of pyrites.

6.4   Ore-forming process

To date, no reliable isotopic age has been obtained for the metallogenic epoch of the Laowan gold deposit because no suitable minerals have been observed. The Laowan deposit is located in the south-central portion of the Qinling-Dabie orogenic belt on the northern edge of the south China plate. Therefore, we deduce that the formation of the Laowan gold deposit was closely related to the structural evolution of the north China and south China cratons. The garnet amphibolite of the Guishanyan Formation yields an amphibole Ar-Ar age of (401.49±3.8) Ma, suggesting that the Guishanyan Formation was involved in the Caledonian to early Hercynian metamorphic thermal event (Liu et al., 1993). Zhai et al. (1998) also obtained an amphibole Ar-Ar age of (404±4) Ma for the Xinyang and Qinlin Groups. Therefore, 400–408 Ma was the peak metamorphic period in this region. During this time, the

amphibolite and PyI formed. Large-scale magmatic intrusions occurred in the study area in the Yanshanian, forming the Laowan granite ((132.5±2.4) Ma; Liu et al., 2008a) and the Liangwan granite ((132.5±2.3) Ma; Jiang et al., 2009). The mineralization time of the Laowan gold deposit obtained by ^{39}Ar-^{40}Ar age of hydrothermal muscovite included in ore veins is (138±2) Ma (Zhang et al., 2008a). The spatial and temporal associations between the Laowan granite and Laowan gold deposit led to speculation that gold mineralization was temporally and genetically related to granite magmatism (Xie et al., 2000; Zhang et al., 2008a; Yang et al., 2015). PyII formed in the initial stage of gold mineralization, with minor gold minerals. PyIII, which contains micron-scale visible gold and less invisible gold, formed during this stage from a mixture of meteoric and magmatic hydrothermal fluids. Its S isotopes also indicate a mixture of magmatic and strata sulfur. The involvement of meteoric water led to the third stage of mineralization in the Laowan gold deposit. PyIV, which contains the highest visible gold content, exhibits the characteristics of magmatic pyrite which was precipitated from an ore-forming fluid derived from a mixture of meteoric and magmatic water.

Previous studies have suggested that the Guishanyan Formation is generally gold-bearing. The Au and Ag concentrations of its two-mica quartz schist and plagioclase amphibole schist are 0.08×10^{-6} and 0.08×10^{-6} and 2.14×10^{-6} and 2.2×10^{-6}, respectively. Note that the Laowan granite and its associated dike rocks have no Au or Ag and that gold and silver are only present where they have intruded schists (Ding and Wang, 2014). The S, H, and O isotope data show that the S isotopes in the pyrites that formed during the three stages of mineralization were derived from strata and the Laowan granite. Their ore-forming fluids were primarily derived from magma during the early stage of mineralization. Meteoric water was added later. Therefore, these data suggest the following possible mineralization process: when the Laowan granite intruded the strata, the magmatic fluid reacted with the wall rock and extracted Au and Ag. PyII, which has a highly invisible gold concentration, was formed during this stage. With the evolution of the mineralization process, the magmatic water reacted with the early minerals and extracted the invisible gold from PyII, which facilitated the further enrichment of Au in the fluid. During the migration of Au-bearing fluid, a small amount of meteoric water was added, which changed the temperature and pressure of the ore-forming fluid. The changed physicochemical conditions might have caused Au to precipitate in the fissures and cracks of PyIII. In mineralization Stage III, more meteoric water was added. The changes in temperature and pressure might have caused more Cu, Zn, and Pb to precipitate from the ore-forming fluid (Zhao et al., 2011; Hu et al., 2019). During this stage, more visible gold precipitated in the fissures and cracks of PyIV and other sulfides, such as chalcopyrite, sphalerite, and galena. At the end of the metallogenic stage, a large amount of meteoric water was added, which further decreased the ore-forming temperature and formed the gold-free pyrite PyV. Thus, we conclude that the Laowan gold deposit is related to the magmatic hydrothermal fluid.

7 Conclusions

Pyrite is widely developed in the study area and can be divided into five generations: one that formed during the metamorphic-diagenetic epoch (PyI) and four that formed during the metallogenic epoch (PyII, PyIII, PyIV, and PyV). PyI contains almost no Au, indicating that no gold mineralization occurred during the diagenetic epoch. In the mineralization stages, Au and Ag are present as visible native gold and electrum, some of which also occur as an invisible solid solution or nanoparticles in the pyrite crystal lattice. Furthermore, the positive correlations between Ag and Pb and Sb and Bi demonstrate that Ag may occur as S-Sb compounds (e.g., argyrythrose) in galena.

The H and O isotope data show that the ore-forming fluids of the Laowan gold deposit exhibit the characteristics of mixing between magmatic water and meteoric water. In Stage I, the ore-forming fluids were mainly derived from magma. In Stages II and III, some meteoric water was added to these fluids. In Stage IV, the ore-forming fluid was primarily composed of meteoric water. The S isotopes of pyrites indicate that the hydrothermal fluids present during diagenesis were different from those present during mineralization and the sulfur was derived from both the Guishanyan Formation and the Laowan granite.

The observed Co/Ni values and Se concentrations indicate that PyI in the metamorphic-diagenetic stage mainly reflects metamorphic sedimentary genesis. The pyrites in the ore-forming stages mostly reflect hydrothermal genesis implying that magmatic water was added during their formation. Thus, we conclude that the Laowan gold deposit is related to the magmatic hydrothermal fluid.

References

Bralia A, Sabatini G, Troja F (1979). A revaluation of the Co/Ni ratio in pyrite as geochemical tool in ore genesis problems. Miner Depos, 14 (3): 353–374

Chen L, Dai L J, Wang T J, Luo P, Xia G T (2009). Geochemical characteristics and genesis of the Laowan gold deposit in Henan

Province. Geosci, 23(2): 277–284

Chen J L (2017). Genesis and significance in ore prospecting of LaoWan gold deposit, Tongbai region, Henan Province. Dissertation for the Master's Degree. Wuhan: China University of Geosciences (in Chinese)

Chou G L, Chen Q, Liu J T (1983). On mélange in the area of Xinyang-Tongbai. J. Changchun Institute Geol, (2): 47–56

Clayton R N, O'Neil J R, Mayeda T K (1972). Oxygen isotope exchange between quartz and water. J Geophys Res, 77(17): 3057–3067

Coleman M L, Shepherd T J, Durham J J, Rouse J E, Moore G R (1982). Reduction of water with zinc for hydrogen isotope analysis. Anal Chem, 54: 993–995

Cook N J, Ciobanu C L, Mao J W (2009). Textural control on gold distribution in As-free pyrite from the Dongping, Huangtuliang and Hougou gold deposits, north China craton (Hebei Province, China). Chem Geol, 264(1–4): 101–121

Cook N J, Spry P G, Vokes F M (1998). Mineralogy and textural relationships among sulphosalts and related minerals in the Bleikvassli Zn–Pb–(Cu) deposit, Nordland, Norway. Miner Depos, 34(1): 35–56

Ding L, Wang G X (2014). The mineralization characteristic and analysis of the Laowan gold deposit in the Tongbai region, Henan. Geol Chem Mineral, 36(1): 13–23

Dong L L, Wan B, Deng C, Cai K D, Xiao W J (2018). An Early Permian epithermal gold system in the Tulasu Basin in North Xinjiang, NW China: constraints from *in situ* oxygen-sulfur isotopes and geochronology. J Asian Earth Sci, 153: 412–424

Dong Y P, Zhou M F, Zhang G W, Zhou D W, Liu L, Zhang Q (2008). The Grenvillian Songshugou ophiolite in the Qinling Mountains, Central China: implications for the tectonic evolution of the Qinling orogenic belt. J Asian Earth Sci, 32(5): 325–335

Fang G S, Hou H Y (2004). Geochemical characteristic of Laowan deposit in Tongbai, Henan Province. Hubei Geol & Miner Res, 18(2): 23–29

Faure K (2003). δD values of fluid inclusion water in quartz and calcite ejecta from active geothermal systems: do values reflect those of original hydrothermal water? Econ Geol, 98(3): 657–660

Gao H M (1989). Preliminary summary of geological characteristics of Laowan gold deposit. Henan Geol, 7(1): 1–5

Goldfarb R J, Ayuso R, Miller M L, Ebert S W, Marsh E E, Petsel S A, Miller L D, Bradley D, Johnson C, McClelland W (2004). The Late Cretaceous Donlin Creek gold deposit, Southwestern Alaska: Controls on epizonal ore formation. Econ Geol, 99(4): 643–671

He X L, Wang H E (2005). The metallogenic relation between Laowan rock mass and Laowan gold belt in Tongbai County of Henan. Res Envi & Engin, 19(2): 70–75

Henan Geology and Mineral Bureau (1989). Regional Geology of Henan Province. Beijing: Geological Publishing House (in Chinese)

Hu X K, Tang L, Zhang S T, Santosh M, Spencer C J, Zhao Y, Cao H W, Pei Q M (2019). *In situ* trace element and sulfur isotope of pyrite constrain ore genesis in the Shapoling molybdenum deposit, East Qinling Orogen, China. Ore Geol Rev, 105: 123–136

Hu Z, Zhang W, Liu Y, Gao S, Li M, Zong K, Chen H, Hu S (2015). "Wave" signal-smoothing and mercury-removing device for laser ablation quadrupole and multiple collector ICPMS analysis: application to lead isotope analysis. Anal Chem, 87(2): 1152–1157

Huerta-Diaz M A, Morse J W (1992). Pyritization of trace metals in anoxic marine sediments. Geochim Cosmochim Acta, 56(7): 2681–2702

Jiang S H, Nie F J, Fang D H, Liu Y F (2009). Geochronology and geochemical features of the main intrusive rocks in the Weishancheng area, Tongbai County, Henan. Acta Geol Sin, 83(7): 1011–1029

Koglin N, Frimmel H E, Lawrie Minter W E, Brätz H (2010). Trace-element characteristics of different pyrite types in Mesoarchaean to Palaeoproterozoic placer deposits. Miner Depos, 45(3): 259–280

Kou S L (2016). Geology and ore-forming fluid geochemistry of the Shangshanghe segment of the Laowan gold deposit, Tongbai County of Henan Province, China. Dissertation for the Master's Degree. Beijing: China University of Geosciences (in Chinese)

Kou S L, Du Y S, Cao Y, Chen J L, Shi G M, Chen J D, Wang L H (2016). Geology and ore-forming fluid geochemistry of Laowan gold deposit in Tongbai County, Henan Province. Miner Depos, 35(2): 245–260

Kröner A, Zhang G W, Sun Y (1993) Granulites in the Tongbai area, Qinling belt, China: geochemistry, petrology, single zircon geochronology, and implications for the tectonic evolution of eastern Asia. Tectonics, 12: 245–255

Large R R, Danyushevsky L, Hollit C, Maslennikov V, Meffre S, Gilbert S, Bull S, Scott R, Emsbo P, Thomas H, Singh B, Foster J (2009). Gold and trace element zonation in pyrite using a laser imaging technique: implications for the timing of gold in orogenic and Carlin-style sediment-hosted deposits. Econ Geol, 104(5): 635–668

Large R R, Maslennikov V, Robert F, Danyushevsky L V, Chang Z S (2007). Multistage sedimentary and metamorphic origin of pyrite and gold in the Giant Sukhoi Log Deposit, Lena Gold Province, Russia. Econ Geol, 102(7): 1233–1267

Li H M (2007). Study on the sources of ore-forming materials in the major gold-silver-polymetal doposits in Tongbai County, Henan Province, China. Dissertation for the Master's Degree. Beijing: China University of Geosciences (in Chinese)

Li J, Chen Y J, Liu Y X (2004). Typomorphic characteristics of pyrite from lode gold deposits in north China craton: implications for fluid mineralization. J Miner Petrol, 24(3): 93–102

Li X, Zhao K D, Jiang S Y, Palmer M R (2019). *In-situ* U-Pb geochronology and sulfur isotopes constrain the metallogenesis of the giant Neves Corvo deposit, Iberian Pyrite Belt. Ore Geol Rev, 105: 223–235

Lin R H, Wang T J, Shi G W, Wang J (2010). Structure control characteristics and genesis of Laowan gold deposit in Henan province. Contrib Geol Mineral Reso Res, 25(4): 342–346

Liu W C, Du J G, Zhang D, Mao X C (2003). The relationship between structures and mineralization of Laowan gold mining area in northern Huaiyang tectonic belt. Geosci, 17(1): 8–19

Liu X C, Jahn B M, Cui J J, Li S Z, Wu Y B, Li X H (2010). Triassic retrograded eclogites and Cretaceous gneissic granites in the Tongbai Complex, central China: implications for the architecture of the HP/UHP Tongbai–Dabie–Sulu collision zone. Lithos, 119(3–4): 211–237

Liu X C, Jahn B M, Hu J, Li S Z, Liu X, Song B (2011). Metamorphic patterns and SHRIMP zircon ages of medium-to-high grade rocks from the Tongbai orogen, central China: implications for multiple

accretion/collision processes prior to terminal continental collision. J Metamorph Geol, 29(9): 979–1002

Liu Y F, Jiang S H, Fang D H, Liu Y (2008a). Zircon SHRIMP U-Pb dating of Laowan granite in Tongbai area, Henan Province, and its geological implications. Acta Petrol Miner, 27(6): 33–37

Liu Y J, Cao L M, Li Z L, Wang H N, Chu T Q, Zhang J R (1984). Element Geochemistry. Beijing: Geological Publishing House (in Chinese)

Liu Y S, Hu Z C, Gao S, Günther D, Xu J, Gao C G, Chen H H (2008b). In situ analysis of major and trace elements of anhydrous minerals by LA-ICP-MS without applying an internal standard. Chem Geol, 257 (1–2): 34–43

Liu Q, Zhu R, Pan Y, Guo B (1999). Secular variations in geomagnetic field caused by the fluctuations in the fluid flow in the outer-core. Chin Sci Bull, 44(13): 1214–1218

Loftus-Hills G, Solomon M (1967). Cobalt, nickel and selenium in sulphides as indicators of ore genesis. Miner Depos, 2: 228–242

Ma H W (2007). Integrated ore-prospecting criteria and ore-prospecting model for the Laowan gold deposit in Tonbai County, Henan province. Geophys Geochem Explor, 31(3): 211–215

Maslennikov V V, Maslennikova S P, Large R R, Danyushevsky L V (2009). Study of trace element zonation in vent chimneys from the Silurian Yaman-Kasay volcanic-hosted massive sulfide deposit (southern Urals, Russia) using laser ablation-inductively coupled plasma mass spectrometry (LA-ICPMS). Econ Geol, 104(8): 1111–1141

Mills S E, Tomkins A G, Weinberg R F, Fan H R (2015). Implications of pyrite geochemistry for gold mineralisation and remobilisation in the Jiaodong gold district, northeast China. Ore Geol Rev, 71: 150–168

Morse J W, Luther G W III (1999). Chemical influences on trace metal-sulfide interactions in anoxic sediments. Geochim Cosmochim Acta, 63(19–20): 3373–3378

Mumin A H, Fleet M E, Chryssoulis S L (1994). Gold mineralisation in As-rich mesothermal gold ores of the Bogosu–Prestea mining district of the Ashanti gold belt, Ghana: remobilization of "invisible" gold. Miner Depos, 29(6): 445–460

Niu B, Liu Z, Ren J (1993) The tectonic relationship between the Qinling Mountains and Tongbai-Dabie Mountains with notes on the tectonic evolution of the Hehuai Basin. Bull Chin Academy Geol Sci, 26:1–12

Ohmoto H (1986). Stable isotope geochemistry of ore deposits. Rev Mineral, 16: 491–559

Ohmoto H, Goldhaber M B (1997). Sulfur and carbon isotopes. In: Barnes HL ed. Geochemistry of Hydrothermal Ore Deposits, 3rd ed. New York: Wiley, 435–486

Palenik C S, Utsunomiya S, Reich M, Kesler S E, Wang L M, Ewing R C (2004). "Invisible" Gold revealed: direct imaging of gold nanoparticles in a Carlin-type deposit. Am Mineral, 89(10): 1359–1366

Pan C R (1999). Laowan gold deposit and mineralization dynamic of magmatic hydrothermal in Tongbai, Henan Province, China. Dissertation for the Master's Degree. Hefei: Hefei University of Technology (in Chinese)

Pan C R, Yue S C (2002). Research on the forming era of Laowan gold deposit in Henan Province and its lead isotope. J Hefei Uni Technol, 25(1): 9–13

Pirajno F (2007). Diagnostic fluid inclusions of different types hydrothermal gold deposits. Acta Petrol Sin, 23(9): 2085–2108

Price B J (1972). Minor elements in pyrites from the Smithers map area, British Columbia and exploration applications of minor element studies. Dissertation for the Master's Degree. Vancouver: University of British Columbia

Reich M, Kesler S E, Utsunomiya S, Palenik C S, Chryssoulis S L, Ewing R C (2005). Solubility of gold in arsenian pyrite. Geochim Cosmochim Acta, 69(11): 2781–2796

Reich M, Utsunomiya S, Kesler S E, Wang L, Ewing R C, Becker U (2006). Thermal behavior of metal nanoparticles in geologic materials. Geology, 34(12): 1033–1036

Shao J (1995). Geology setting of Laowan Au-mineralization zone. J Precious Metallic Geol, 4 (2): 138–146

Sheppard S M F (1986). Characterization and isotopic variations in natural waters. Rev Mineral, 16: 165–183

Song X X (1984). Minor elements and ore genesis of the fankou lead-zinc deposit, China. Miner Depos, 19(2): 95–104

Song X X, Zhang J K (1986). Minor elements in pyrites of various genetic types from China. Bull Institute Miner Deposits Chin Academy Geolo Sci., 2: 166–175

Sung Y H, Brugger J, Ciobanu C L, Pring A, Skinner W, Nugus M (2009). Invisible gold in arsenian pyrite and arsenopyrite from a multistage Archaean gold deposit: Sunrise Dam, eastern goldfields province, Western Australia. Miner Depos, 44(7): 765–791

Suo S T, Zhang W J (1993). On a two-side orogeny—an example taking from the Tongbai-Dabie orogenic belt. J Xi'an College Geol, 15(s1): 29–37

Suo S T, Zhong Z Q, Wei B Z, Zhang H F, Zhou H W, You Z D (2002). Structure and rheological evolution of UHP and HP metamorphic belts in the Tongbai-Dabie-Sulu region, China. Earth Sci J China Uni Geosci, 27(5): 549–557

Suo S T, Zhong Z Q, Zhang H F, Zhou H W, You Z D (2001). High-pressure metamorphic and its tectonic pattern in Tongbai Mountains, central China. Earth Sci J China Uni Geosci, 26(6): 551–559

Taylor H P J (1997). Oxygen and hydrogen isotope relationships in hydrothermal mineral deposits. Geochem Hydrothermal Ore Depos, 229–302

Tribovillard N, Algeo T J, Lyons T, Riboulleau A (2006). Trace metals as paleoredox and paleoproductivity proxies: an update. Chem Geol, 232(1–2): 12–32

Vikent'ev I V, Sidorova N V, Vikent'eva O V, Su S G, Luo Z H, Bortnikov N S (2015). Tellurides in the Laowan gold deposit (east China): new evidence for a magmatic source of hydrothermal fluids. Dokl Akad Nauk, 462(4): 456–460

Wang S Q, Xu Y L (2005). Research on source of ore-forming materials of Laowan gold deposit in Tongbai County, Henan Province. Express in Formation of Mining Industry, 21(9): 12–14

Wang Z Q, Yan Z, Wang T, Gao L D, Yan Q R, Chen J L, Li Q G, Jiang C F, Liu P, Zhang Y L, Xie C L, Xiang Z J (2009). New advances in the study on ages of metamorphic strata in the Qinling orogenic belt. Acta Geoscientica Sinica, 30(5): 561–570

Xie Q Q, Pan C R, Xu X C, Yue S C (2003). Geochemistry of fluid inclusions and rare earth elements from Laowan gold deposit in Henan Province. J Hefei Uni Technol, 26(1): 47–52

Xie Q Q, Xu X C, Yue S C (2000). Isochron age of the Laowan gold

deposit and Laowan granite, Tongbai region, Henan Province and its implications. Geol J China Uni, 6(4): 546–553

Xie Q Q, Xu X C, Yue S C (2001). Isotopic geochemical of hydrogen, oxygen and helium and ore-forming fluid sources of Laowan gold deposit in Tongbai, Henan Province. Chin J Geol, 36(1): 36–42

Xie Q Q, Xu X C, Li X X, Chen T H, Lu S M (2005). Rare earth element geochemical characteristics of Laowan gold deposit in Henan Province: trace to source of ore-forming materials. J Chin Rare Earth Soci, 23(5): 636–640

Xing B, Zheng W, Ouyang Z X, Wu X D, Lin W P, Tian Y (2016). Sulfide Microanalysis and S isotope of Miaoshan Cu polymetallic deposit in western Guangdong Province, and its constraints on the ore genesis. Acta Geol Sin, 90(5): 971–986

Yan Y T, Zhang N, Li S R, Li Y R (2014). Mineral chemistry and isotope geochemistry of pyrite from the Heilangou gold deposit, Jiaodong Peninsula, eastern China. Geoscience Frontiers, 5(2): 205–213

Yang M Z, Fu J J, Ren A Q (2015). Recognition of Yanshanian magmatic-hydrothermal gold and polymetallic gold mineralization in the Laowan gold metallogenic belt, Tongbai Mountains: new evidence from structural controls, geochronology and geochemistry. Ore Geol Rev, 69: 58–72

Yang M Z, Fu J J, Wang S F, Lu J P (2014a). Establishment and significance of dextral strike-slip fault ore-controlling system of the Laowan gold belt. Tongbai Mountains Geotecton Metall, 38(1): 94–107

Yang M Z, Lu J P, Fu J J, Ren A Q, Wang S F (2014b). Magmatic hydrothermal gold and polymetallic metallogenesis related to Yanshanian magmatism of Laowan gold belt, Tongbai Mountain: evidence from geochemistry, geochronology and ore-controlling structural geological constraints. Miner Depos, 33(3): 651–666

Yuan D Y, Li Y D (2008). Study on the alteration characteristics of the surrounding rock of Laowan gold deposit in Tongbai County, Henan. Express Information of Mining Industry, 24(7): 78–79

Zhai X, Day H W, Hacker B R, You Z (1998). Paleozoic metamorphism in the Qinling orogen, Tongbai Mountains, central China. Geology, 26(4): 371

Zhang G, Li H M, Wang C H, Wang D H, Li L X, Zhang J (2008a). ^{40}Ar–^{39}Ar age of muscovite from the Laowan gold deposit in Henan and its significance. Acta Geoscientica Sinica, 29(1): 45–50 (in Chinese)

Zhang G, Wang D H, Li F L (2008b). Laowan granitic body and association genesis of Laowan gold deposit in the eastern Qinling. Geol Prospect, 44(4): 50–54

Zhang G, Yu Z, Sun Y, Cheng S, Li T, Xue F, Zhang C (1989). The major suture zone of the Qinling orogenic belt. Southeast Asian Earth

Sci, 3: 63–76

Zhang H, Song C Z, Wang D X, Ren S L, Tu W C, Li J H (2012). Temperature and pressure conditions of tectonic deformation of Zhuyangguan-Xiaguan fault belt. J Hefei Uni Technol, 35(8): 1101–1105

Zhang J, Deng J, Chen H Y, Yang L Q L, Cooke D, Danyushevsky L, Gong Q J (2014). LA-ICP-MS trace element analysis of pyrite from the Chang'an gold deposit, Sanjiang region, China: implication for ore-forming process. Gondwana Res, 26(2): 557–575

Zhang S G, Wan Y S, Liu G H (1991). Metamorphic Geology of the Kuanping Group in the Northern Qinling Mountains. Beijing: Sci Technology Press

Zhang Z H, Fang G S, Hou H Y, Ma H W, Hou W R (2002). Geological features and genesis of the Laowan gold deposite in the Tongbai region, Henan. G Geol, 8(3): 20–26

Zhang Z Q, Liu D Y, Fu G M (1994). Isotopic Geochronology of Metamorphic Strata in North Qinling. Beijing: Geological Publishing House

Zhao H X, Frimmel H E, Jiang S Y, Dai B Z (2011). LA-ICP-MS trace element analysis of pyrite from the Xiaoqinling gold district, China: implications for ore genesis. Ore Geol Rev, 43(1): 142–153

Zhao J H (2007). Study on the ore prospecting model and indicator in the Tongbai Dabie orogenic belt gold (silver) ore region. Express Information of Mining Industry, 23(9): 71–73

Zhao J Z (1990). Laowan gold belt and its exploration process. Henan Geol, 8(2): 15–22

Zheng Y F, Chen J F (2000). Stable Isotope Geochemistry. 2nd ed. Beijing: Science Press (in Chinese)

Zheng Y, Zhang L, Chen Y J, Hollings P, Chen H Y (2013). Metamorphosed Pb–Zn–(Ag) ores of the Keketale VMS deposit, NW China: evidence from ore textures, fluid inclusions, geochronology and pyrite compositions. Ore Geol Rev, 54(8): 167–180

Zhong Z Q, Suo S T, Zhang H F, Zhou H W (2001). Major constituents and texture of the Tongbai-Dabie collisional orogenic belt. Earth Sci J China Uni Geosci, 26(6): 560–567

Zhou Q (2016). The prospecting breakthrough of Laowan gold deposit, Henan Province. China Mine Engineering, 45(5): 86

Zhou T F, Zhang L J, Yuan F, Fan Y, Cooke D R (2010). LA-ICP-MS *in situ* trace element analysis of pyrite from the Xinqiao Cu-Au-S deposit in Tongling, Anhui, and its constraints on the ore genesis. Earth Sci Front, 17(2): 306–319

Zhu Z Y, Cook N J, Yang T, Ciobanu C L, Zhao K D, Jiang S Y (2016). Mapping of sulfur isotopes and trace elements in sulfides by LA-(MC)-ICP-MS: potential analytical problems, improvements and implications. Minerals (Basel), 6(4): 110